

# Engineering Journal



American Institute of Steel Construction

Second Quarter 2016 Volume 53, No. 2

- 73 Design of Horizontal Life Lines in Personal  
Fall Arrest Systems  
Thomas S. Dranger
- 87 Tensile Strength of Embedded Anchor Groups:  
Tests and Strength Models  
David A. Grilli and Amit M. Kanvinde
- 99 Cross-Section Strength of Circular Concrete-Filled  
Steel Tube Beam-Columns  
Mark D. Denavit, Jerome F. Hajjar and Roberto T. Leon
- 107 Design for Deconstruction with Demountable  
Composite Beams and Floor Systems  
Judy Liu

# Design of Horizontal Life Lines in Personal Fall Arrest Systems

THOMAS S. DRANGER

---

## ABSTRACT

Personal fall arrest systems have become common in construction, maintenance, and many other activities including recreation. Many use a horizontal lifeline (HLL), often a steel cable. Their design is governed by Occupational Safety and Health Administration (OSHA) regulations that require “supervision by a qualified person” and a factor of safety of at least two. In contrast to a vertical lifeline that can be analyzed as a linear spring, a HLL has non-linear elastic behavior. The analysis is complicated by the fact that both the maximum arresting force and the geometric shape of the HLL at the stopping point are initially unknown. Some suggestions for estimating the arresting forces are known to be grossly in error for the general case. Greater confidence in a design is realized when arresting forces are found by rational analysis. This paper gives a summary of regulations, a reiterative method of analysis, a discussion of the limit states, and some appropriate modifications in the case of unacceptable behavior. The effects of assumptions used in the analysis are discussed in the conclusion.

**Keywords:** horizontal lifeline, personal fall arrest systems, Occupational Safety and Health Administration, harness and lanyard, steel cable, galvanized aircraft cable, life safety, fall protection.

---

## INTRODUCTION

Personal fall arrest systems (PFASs) are a topic of great importance in the construction industry as well as recreational facilities such as high ropes challenge courses. The Occupational Safety and Health Administration (OSHA) governs the design of such systems used by employees, and few engineers or lawyers would concede that any person in the same environment should have less protection simply because they are not employees. Many component parts of PFASs are readily available in high-quality, ready-made products, partly because the loads they are expected to sustain and the way they are used have little variation from site to site, and their designs can be tested before manufacture. Such is not the case for a horizontal lifeline (HLL). Kits for constructing HLLs within certain limitations are commercially available but are not for universal use. Some rely on proprietary components such as “impact attenuators” that make their analysis difficult. HLLs should be validated for use in the specific case before they are placed in service. The engineer responsible for the specification of HLLs may want to check the design of a proposed HLL or complete a design from scratch.

One publication by the Association for Challenge Course Technology (ACCT, 2012) referring to a PFAS using an HLL with a relatively short span (as opposed to a zipline) supported by guyed poles, states that “a single person may generate a vertical load up to 500 lbf (2.2 kN) under normal operating conditions” and goes on to analyze an HLL with 5% sag under the assumed arresting load. This HLL is similar to the one analyzed in Example 2 herein, where the calculated arresting force of 1.57 kip does not agree with the arresting force recommended in the ACCT standard.

In a field test performed on August 26, 2014 (Jacobs, private correspondence), that used a plastic dummy filled with 300 lb of steel ball bearings and water arrested by an HLL of newly installed, non-prestretched  $\frac{3}{8}$ -in. galvanized aircraft cable (GAC) with a specified initial sag of 6% spanning 25.7 ft between guyed poles, the arresting forces recorded by a load cell for three drops were 763, 862 and 807 lb. The field test does not agree with the arresting force recommended in the ACCT standard.

Designers looking for guidance may find statements such as, “If the lifeline is tight, it won’t sag much when a fall occurs, but the impact force on the lifeline will be high.” This appeared in a text used for training (OSHAcademy, n.d.) until a recent modification. Possibly, this refers to tension in the HLL, but, even as a rule of thumb, it is untrue and possibly dangerous if interpreted as the arresting force on the falling person.

Perceiving a need for clarity, a rational method for design of HLLs adaptable to many configurations is presented herein with examples.

---

Thomas S. Dranger, Ph.D., S.E., P.E., Consulting Engineer, Sauk Village, IL.  
Email: dranger@thomasengineers.com

---

Paper No. 2014-25R

## DEFINITIONS AND DESIGN CRITERIA

Not every provision of OSHA 1926 (n.d. a), which governs many details in a PFAS, will be included in this paper. The focus will be on compliance with OSHA 1926.502(d)(8): “Horizontal lifelines shall be designed, installed, and used, under the supervision of a qualified person, as part of a complete personal fall arrest system, which maintains a safety factor of at least two.” Referring to OSHA 1926.32(m), “Qualified” means one who, “by possession of a recognized degree, certificate, or professional standing, or who by extensive knowledge, training, and experience, has successfully demonstrated his ability to solve or resolve problems relating to the subject matter, the work, or the project.” The design of HLLs is within the discipline of structural engineering in that “safe design and construction require that loads and stresses must be computed and the size and strength of parts determined by mathematical calculations based upon scientific principles and engineering data” (State of Illinois, 1989).

To describe a PFAS, these three definitions appear in the OSHA (n.d. b) glossary:

**Personal fall arrest system:** A system used to stop an employee in a fall from a working level. It consists of an anchorage, connectors, a body harness, and may include a lanyard, deceleration device, lifeline, or suitable combinations of these.

**Lanyard:** A flexible line of rope, wire rope, or strap which generally has a connector at each end for connecting the body belt or body harness to a deceleration device, lifeline, or anchorage.

**Lifeline:** A component consisting of a flexible line connected vertically to an anchorage at one end (vertical lifeline), or connected horizontally to anchorages at both ends (horizontal lifeline), and which serves as a means for connecting other components of a personal fall arrest system to the anchorage.

These are a few pertinent OSHA (n.d. a) requirements regarding free fall, arresting distance and force:

1926.502(d)(12) Self-retracting lifelines and lanyards which automatically limit free fall distance to 2 feet (0.61 m) or less shall be capable of sustaining a minimum tensile load of 3,000 pounds (13.3 kN) applied to the device with the lifeline or lanyard in the fully extended position.

1926.502(d)(16) Personal fall arrest systems, when stopping a fall, shall:

1926.502(d)(16)(ii) limit maximum arresting force on an employee to 1,800 pounds (8 kN) [about 6 g’s] ... ;

1926.502(d)(16)(iii) be rigged such that an employee

can neither free fall more than 6 feet (1.8 m), nor contact any lower level;

1926.502(d)(16)(iv) bring an employee to a complete stop and limit maximum deceleration distance an employee travels to 3.5 feet (1.07 m); and ...

1926.502(d)(16)(v) have sufficient strength to withstand twice the potential impact energy of an employee free falling a distance of 6 feet (1.8 m), or the free fall distance permitted by the system, whichever is less.

Note: If the personal fall arrest system meets the criteria and protocols contained in Appendix C to subpart M, and if the system is being used by an employee having a combined person and tool weight of less than 310 pounds (140 kg), the system will be considered to be in compliance with the provisions of paragraph (d)(16) of this section. If the system is used by an employee having a combined tool and body weight of 310 pounds (140 kg) or more, then the employer must appropriately modify the criteria and protocols of the Appendix to provide proper protection for such heavier weights, or the system will not be deemed to be in compliance with the requirements of paragraph (d)(16) of this section.

## DESIGN OVERVIEW

Consider a person fitted with a harness connected by a lanyard running along a horizontal lifeline anchored at both ends to supporting structures that may be rigid or elastic, thus protected from falling to a surface below his position at work. There is usually some slack in both the lanyard and the HLL, allowing some distance of vertical free fall from initial position until the slack is taken up. From this point, the arresting (or decelerating) force increases through the arresting distance from zero to a maximum value at the stopping point. The shape of a HLL under its own weight is a catenary, changing to a shallow V when the slack is taken up, and a deepening V as the fall is arrested. The HLL is a nonlinear spring. After reaching the low point, there will be some rebound and dissipation of energy, reducing the dynamic forces to zero. This subsequent behavior is not investigated because all the forces within the PFAS are greatest at the low point.

The design problem is stated thus: Given the weight of the falling person, the free-fall distance, and the spring constants of the supports, determine the proper material properties, span and initial sag of the HLL so that the arresting distance and maximum arresting force are acceptable and the limit states of the HLL are not exceeded. The method of solution given here will assume a value of tension in the HLL, determine the deflected shape that satisfies statics and compatibility, and then check that limit states (including

restrictions on arresting force and stopping distance) are satisfied. All objects and parts of the system are assumed to be stationary at the onset of a fall and again at the instant of lowest position when the fall is arrested. At these two instants, the kinetic energy is zero. The change in potential energy will be compared with the change in strain energy within the PFAS. The principle of conservation of energy requires that these two must be equal. If not, the assumed tension in the HLL is adjusted until the correct solution is found. Assumptions, including those already stated, are as follows:

- The weight of the HLL is small compared with the falling person and may be treated as a concentrated load equal to half the cable weight coincident with the location of the falling object, or even neglected.
- Persons are represented by a rigid object having mass at a single point.
- Except for the falling object, inertia within the PFAS is ignored.
- Kinetic energy is zero at the onset of a fall and at the low point.
- No energy is dissipated before reaching the low point of a fall.
- Lanyards, ropes and cables, and horizontal supports of HLLs are linearly elastic.
- The tension in a HLL is the same throughout its length.
- Only one object falls at any given time.
- The spring constant of lanyards is large enough that strain energy within a lanyard can be neglected.
- The trajectory of a falling object and its lanyard are vertical and located at midspan of the HLL.
- There are no other objects supported by a HLL at the time of a fall.

Falls may occur anywhere in the span of an HLL. There are reports that one person falling may precipitate subsequent falls by one or more others. It is not unreasonable to suppose more conservatively that a lifeline may support some previously fallen person while another fall is arrested.

The designer can specify the cable used for the HLL, but there may be a strong preference for some product available from existing stock. The supports may be at predetermined points. Supports may be rigid, or there may be a horizontal spring constant associated with the supports, especially with support by poles or long HLLs passing through intermediate vertical supports. The body harness and lanyard may be the product preferred by the user. The designer should consider

the worst case.

A designer may have more discretion in specifying the sag of the HLL. Too little sag results in high cable tension, even for small loads. Too much may result in excessive arresting force. From experience, 10 to 12% of span is needed for the initial V-shaped sag at midspan. This is converted to unloaded catenary sag for installation and perhaps for a specification for installation tension in the unloaded HLL, measurable by a mechanical tensionometer. Installations with less initial sag, 3% or less, are possible, depending on loads and load combinations, configuration and use of special equipment. A breakaway retainer may be used to tighten the HLL until a fall occurs. Whatever the initial sag, its effect should be determined by analysis.

Galvanized aircraft cable (rarely used in aircraft) may be chosen for HLLs because of its flexibility and other desirable properties. GAC 7 × 19 meeting ASTM A1023 (ASTM, 2009) and federal specification RR-W-410E (GSA, 2007) is available in diameters from  $\frac{3}{32}$  to  $\frac{3}{8}$  in. The 7 × 19 construction means there are 7 strands of 19 wires each in the cable. The wires should be individually galvanized before they are assembled in the cable. Swaged connections can develop 100% of the tensile breaking strength; other mechanical connections can develop not more than 80%.

The properties of rope and cable used in HLLs are not the same as the properties of solid bars of the same material. Because of the spaces between the fibers, the effective cross-section area may be something like 60% of the gross area. The nominal area is the area of a circumscribed circle. The nominal area is greater than the metallic area. Because the arrangement of fibers or wires tightens under tension, the effective modulus of elasticity of a steel cable may be as low as 18,000 to 20,000 ksi. In addition to elastic behavior, there is some amount of inelastic elongation of newly made cable due to compaction when first loaded, perhaps 1%. If prestretched cable is not specified, the initial sag can be made somewhat less to compensate. For the analysis presented herein, the most important properties are the metallic area and the effective modulus of elasticity, or their product (called *AE* in this paper), and the tensile breaking strength. The value of *AE* may be obtained from the manufacturer, or by testing, preferably before analysis. The ASTM International standards A931, "Standard Test Method for Tension Testing of Wire Ropes and Strand" (ASTM, 2013); A603, "Standard Specification for Zinc-Coated Steel Structural Wire Rope" (ASTM, 2014a); and A586, "Standard Specification for Zinc-Coated Parallel and Helical Steel Wire Structural Strand" (ASTM, 2014b), are pertinent. The required value (not the minimum value) of *AE* should be specified by the designer, and certification of conformance should be required. Compliance ultimately depends on testing. Methods for estimating *AE* are available from suppliers but not recommended. If estimated values of *AE* are used, expedited

redesign might be necessary later when confronted by the properties of the material actually available, which may be inconvenient at that time.

While every configuration will have a solution to the energy equation, the limit states may not be satisfied in some cases. If acceptable limit states cannot be achieved by changing the initial sag or using a different cable, the introduction of devices acting as springs (hereinafter called springs) and dampers in HLLs and lanyards may give better results. Springs in lanyards and dampers are discussed but not analyzed in this paper.

### PROCEDURE FOR ANALYSIS

Determine the configuration of the HLL and gather the information needed to begin the analysis. The equations given with the following definitions are for the arresting force of an object falling at midspan of an HLL. Referring to Figures 1, 2 and 3:

- The following are known when the analysis begins:
  - $AE$  = HLL cable property  
= metallic area times the effective modulus of elasticity, kips
  - $Do$  = free-fall distance, same as slack in PFAS lanyard, ft
  - $Ho$  = initial span of HLL, ft
  - $So$  = initial V-shaped sag at rest, ft
  - $Tn$  = cable breaking strength, kips
  - $Wo$  = weight of a falling person with equipment, kips
- Find the initial length of the unloaded cable,  $Lo$ , and the cable stiffness,  $Ke$ .

$$Lo = \sqrt{4(So)^2 + (Ho)^2} \quad (1)$$

$$Ke = \frac{1}{\left(\frac{Lo}{AE} + \frac{1}{Ks}\right)}, \text{ if spring is included} \quad (2)$$

$$Ke = \frac{AE}{Lo}, \text{ if spring is not included} \quad (3)$$

where

$Ks$  = stiffness of a spring included in a HLL, kip/ft

- Select a trial value of  $T$ , the cable tension when the fall is arrested. This may be a first guess or a better estimate based on previous iterations of the solution.

- Find the elongation,  $e$ , and cable length,  $L$ , under load.

$$e = \frac{LoT}{AE} \quad (4)$$

$$L = e + Lo = Lo\left(1 + \frac{T}{AE}\right) \quad (5)$$

- Find the horizontal reactions,  $F$ .

$$F = T \frac{Ho}{L} \quad (6)$$

[Use Equation 6 for Figures 1 and 2. Use Equation 17 for Figure 3.]

- Find the vertical reactions,  $R$ , and the arresting force,  $P$ .

$$P = 2R = 2\sqrt{T^2 - F^2} \quad (7)$$

- Find the distance,  $H$ , between loaded supports, which may be elastic.

$$H = Ho - F\left(\frac{1}{K_1} + \frac{1}{K_2}\right) \quad (8)$$

where

$K_1, K_2$  = stiffness of horizontal supports, kip/ft

- Find the sag,  $S$ .

$$S = \frac{\sqrt{L^2 - H^2}}{2} \quad (9)$$

- Find the strain energy,  $U$ .

$$U = \left(\frac{1}{2}\right)\left[\frac{T^2}{Ke} + F^2\left(\frac{1}{K_1} + \frac{1}{K_2}\right)\right] \quad (10)$$

- Find the change in potential energy,  $W$ .

$$W = Wo(Do + S - So) \quad (11)$$

- Compare  $U$  and  $W$ . They will be equal when the solution is found.

- If  $U > W$ , return to step 3 and decrease the trial tension  $T$ .
- If  $U < W$ , return to step 3 and increase the trial tension  $T$ .
- If  $U = W$  (or close enough), the value of  $T$  is correct. Go on to check the limit states.

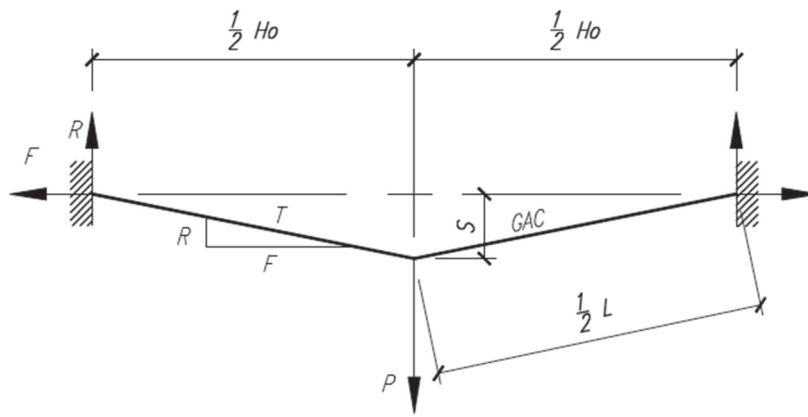


Fig. 1. HLL for Example 1.

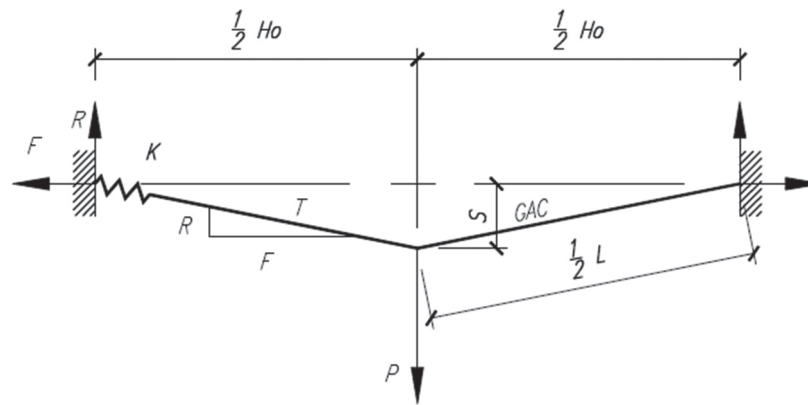


Fig. 2. HLL with spring.

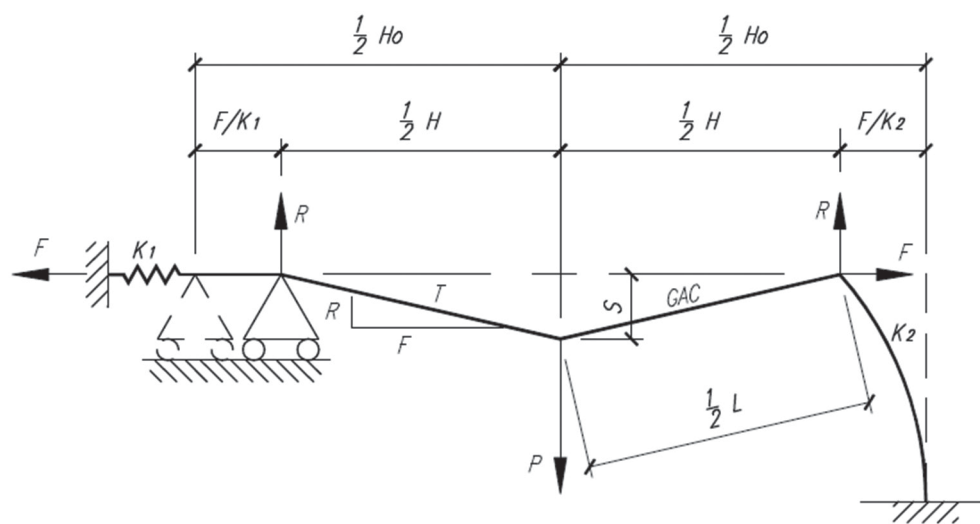


Fig. 3. HLL with elastic horizontal supports.

12. Use  $T$  to check the limit states.

- a. If  $Tn/2 > T$  the cable strength is o.k. Hardware connecting the cable to its supports would also be checked.
- b. Stopping distance  $D_s = S - S_o$  is o.k. if less than 3.5 ft.
- c. Free fall is the slack in the lanyard. Free fall is o.k. if slack  $D_o$  is less than 6 ft.

d. The total fall ( $D_o + D_s$ ) is o.k. if it is less than the distance to obstacles.

e. Arresting force  $P$  is o.k. if it is less than 1,800 lb.

Because there may be many iterations of the solution before converging to the correct value of  $T$  and because a number of configurations may need to be analyzed before arriving at an acceptable design, a spreadsheet is suggested. A spreadsheet should allow changing the initial trial value of  $T$  and the increment in  $T$ , testing perhaps 16 values of  $T$  at a time.

### Example Problem 1

#### Given:

A person is connected by a body harness and lanyard to an HLL of  $\frac{3}{8}$ -in.-diameter  $7 \times 19$  GAC; breaking strength = 14.4 kips, effective rigidity  $AE = 1,004$  kips, span = 30 ft and weight = 310 lb, including equipment (consistent with OSHA). The HLL is connected to rigid horizontal and vertical supports as shown in Figure 1. Slack in the lanyard and HLL will be taken up after a free fall of 2 ft. The initial V-shaped sag is 3.0 ft when the slack is taken up. Analyze the system for a fall at midspan and determine the catenary sag and tension for installation. Ignore the weight of the cable.

1. The following are known when the analysis begins:

$$AE = 1,004 \text{ kips}$$

$$D_o = 2.00 \text{ ft free fall}$$

$$H_o = 30.0 \text{ ft}$$

$$S_o = 3.00 \text{ ft} = 10\% H_o$$

$$T_n = 14.4 \text{ kips for } \frac{3}{8}\text{-in.-diameter } 7 \times 19 \text{ GAC, ASTM A1023}$$

$$W_o = 0.310 \text{ kips, consistent with OSHA for a person with equipment}$$

#### Solution

2. Find the length of the unloaded cable and find the cable stiffness using Equations 1 and 3:

$$\begin{aligned} L_o &= \sqrt{4(S_o)^2 + (H_o)^2} \\ &= \sqrt{4(3.00 \text{ ft})^2 + (30.0 \text{ ft})^2} \\ &= 30.5941 \text{ ft} \end{aligned}$$

$$\begin{aligned} Ke &= \frac{AE}{L_o} \\ &= \frac{1,004 \text{ kips}}{30.5941 \text{ ft}} \\ &= 32.8168 \text{ kip/ft} \end{aligned}$$

3. Try a cable tension of  $T = 7.20$  kips when the fall is arrested. This may be a first guess or a better estimate based on previous iterations of the solution.

4. Find the elongation and cable length under load using Equations 4 and 5:

$$\begin{aligned} e &= \frac{LoT}{AE} \\ &= \frac{(30.5941 \text{ ft})(7.20 \text{ kips})}{1,004 \text{ kips}} \\ &= 0.2194 \text{ ft} \end{aligned}$$

$$\begin{aligned} L &= e + Lo \\ &= 0.2194 \text{ ft} + 30.5941 \text{ ft} \\ &= 30.8135 \text{ ft} \end{aligned}$$

5. Find the horizontal reactions using Equation 6:

$$\begin{aligned} F &= T \frac{Ho}{L} \\ &= (7.20 \text{ kips}) \left( \frac{30.0 \text{ ft}}{30.8135 \text{ ft}} \right) \\ &= 7.0099 \text{ kips} \end{aligned}$$

6. Find the arresting force using Equation 7:

$$\begin{aligned} P &= 2\sqrt{T^2 - F^2} \\ &= 2\sqrt{(7.20 \text{ kips})^2 - (7.0099 \text{ kips})^2} \\ &= 3.2870 \text{ kips} \end{aligned}$$

7. Supports are immovable:

$$\begin{aligned} H &= Ho \\ &= 30.0 \text{ ft} \end{aligned}$$

8. Find the sag using Equation 9:

$$\begin{aligned} S &= \frac{\sqrt{L^2 - H^2}}{2} \\ &= \frac{\sqrt{(30.8135 \text{ ft})^2 - (30.0 \text{ ft})^2}}{2} \\ &= 3.5168 \text{ ft} \end{aligned}$$

9. Find the strain energy using Equation 10:

$$\begin{aligned} U &= \frac{1}{2} \left( \frac{T^2 Lo}{AE} \right) \\ &= \frac{1}{2} \left( \frac{(7.20 \text{ kips})^2 (30.5941 \text{ ft})}{1,004 \text{ kips}} \right) \\ &= 0.7898 \text{ kip-ft} \end{aligned}$$

Table 1. Example 1 $T$ Trials							
$T$ (kips)	$F$ (kips)	$P$ (kips)	$L$ (ft)	$H$ (ft)	$S$ (ft)	$U$ (kip-ft)	$W$ (kip-ft)
7.100	6.913	3.236	30.810	30.00	3.510	0.768	0.778
7.150	6.962	3.261	30.812	30.00	3.514	0.779	0.779
7.200	7.010	3.287	30.814	30.00	3.517	0.790	0.780

10. Find the change in potential energy using Equation 11:

$$\begin{aligned}
 W &= W_o(D_o + S - S_o) \\
 &= (0.310 \text{ kips})(2.00 \text{ ft} + 3.5168 \text{ ft} - 3.00 \text{ ft}) \\
 &= 0.7802 \text{ kip-ft}
 \end{aligned}$$

11. Because  $U > W$ , the trial value of  $T$  is too great. Other values of  $T$  may be tested by returning to step 3. The energy equation balances within 2%; try other values of  $T$  using an increment less than 2%  $T/2$ , say, 0.05 kip. The results of trials of nearby values of  $T$  made with a spreadsheet are summarized in Table 1. From these results, we see that for values of  $T < 7.15$  kip, the calculated strain energy  $U$  is less than the change in potential energy  $W$ . For values of  $T > 7.15$  kip, the calculated strain energy  $U$  is greater than the change in potential energy  $W$ . The correct value of  $T$  is 7.15 kip, resulting in  $U = W = 0.779$  kip-ft.

12. The following limit states will be checked using  $T = 7.15$  kip.

a. The cable strength is checked:

$$Tn/2 = 7.20 \text{ kip} > T = 7.15 \text{ kips} \quad \mathbf{o.k.} \text{ (but very close)}$$

b. Stopping distance is checked:

$$\begin{aligned}
 D_s &= S - S_o \\
 &= 3.514 \text{ ft} - 3.00 \text{ ft} \\
 &= 0.514 \text{ ft} < 3.50 \text{ ft} \quad \mathbf{o.k.}
 \end{aligned}$$

c. Free fall is limited by lanyard slack adjustment:

$$D_o = 2.00 \text{ ft} < 6.00 \text{ ft} \quad \mathbf{o.k.}$$

d. The total fall ( $D_o + D_s$ ) must be checked against distance to obstacles:

$$D_o + D_s = 2.00 \text{ ft} + 0.514 \text{ ft} = 2.514 \text{ ft}$$

e. The arresting force is checked:

$$P = 3.261 \text{ kip} = 3,261 \text{ lb} > 1,800 \text{ lb.} \quad \mathbf{N.G.}$$

The arresting force is too high. Reducing the initial sag will reduce the arresting force but increase the cable tension, which is already very close to the limit. The arresting force can also be reduced by introducing a spring in the lanyard or the HLL, in the horizontal supports of the HLL or by damping (e.g., using a manufactured load limiting energy dissipating device). Manufactured damping devices often operate on the principle that deforming or ripping material dissipates energy, and the length of the device is extended in the process. The energy dissipated by a damping device would be included in  $U$ , and the elongation associated with a damping device would be considered in calculating  $W$ . The force required to activate the device, the energy dissipated, and the maximum extension would be specified by the manufacturer.

### ***Springs in the Horizontal Lifeline***

If a spring is introduced in the HLL attached to rigid supports as in Figure 2, the arresting force will be softened. The effective HLL stiffness,  $Ke$ , of this combination of spring stiffness,  $Ks$ , and cable stiffness,  $AE/Lo$ , is given by:

$$Ke = \frac{1}{\left(\frac{Lo}{AE} + \frac{1}{Ks}\right)} \quad (12)$$

The analysis can proceed as in Example 1 using this modified value of  $Ke$ .

To realize a spring in the HLL, the HLL may take the form of a loop running through sheaves (pulleys) at the two supports. This configuration would nearly double the length of cable and reduce  $Ke$  by nearly one-half. Other configurations to increase the length of cable are also possible.

### ***Elasticity in the Horizontal Supports***

Elasticity in one or both horizontal supports where the horizontal reaction causes the vertical support to move also softens the arresting force. This is the case of an HLL supported by vertical elastic poles. A vertical elastic pole may be a column fixed at the base and free at the top, or it may be guyed at the top. The right support in Figure 3 is a vertical elastic pole, where deflection at the top is proportional to force. The horizontal span of the cable changes under load, and the slope of the cable and the horizontal reaction cannot be determined as in Example 1. It is useful to develop an equation to quickly evaluate the horizontal reaction.

### **Example Problem 2**

#### **Given:**

Repeat Example 1, but one support has a horizontal spring constant of  $K_2 = 2.00$  kip/ft and the initial sag is 5%.

1. The following are known when the analysis begins:

$AE = 1,004$  kips (must be obtained from the manufacturer or determined by testing)

$Do = 2.00$  ft (free-fall)

$Ho = 30.0$  ft

$K_1 = \infty$

$K_2 = 2.00$  kip/ft

$So = 1.50$  ft (= 5%  $Ho$ )

$Tn = 14.4$  kips for  $\frac{3}{8}$ -in.-diameter  $7 \times 19$  GAC, ASTM A1023

$Wo = 0.310$  kips

Suppose the horizontal supports have spring constants  $K_1$  and  $K_2$ . Recall that  $L$  is the length of the elongated cable having tension  $T$ , and let  $H$  be the cable span after movement of the supports.

The horizontal reaction is determined:

$$F = T \left( \frac{H}{L} \right) \quad (13)$$

$$FL = TH \quad (14)$$

The cable span after movement of support due to  $F$  is:

$$H = Ho - F \left( \frac{1}{K_1} + \frac{1}{K_2} \right) \quad (15)$$

Substituting  $H$  from Equation 15 into Equation 14:

$$FL = T \left[ Ho - F \left( \frac{1}{K_1} + \frac{1}{K_2} \right) \right] \quad (16)$$

Solving for  $F$ :

$$F = \frac{Ho}{\left( \frac{L}{T} + \frac{1}{K_1} + \frac{1}{K_2} \right)} \quad (17)$$

**Solution:**

2. Find initial length of cable using Equation 1:

$$\begin{aligned} L_o &= \sqrt{4(S_o)^2 + (H_o)^2} \\ &= \sqrt{4(1.50 \text{ ft})^2 + (30.0 \text{ ft})^2} \\ &= 30.1496 \text{ ft} \end{aligned}$$

3. Try a cable tension of  $T = 2.60$  kips when the fall is arrested.  
 4. Find the elongation and cable length under load using Equations 4 and 5:

$$\begin{aligned} e &= \frac{LoT}{AE} \\ &= \frac{(30.1496 \text{ ft})(2.60 \text{ kips})}{1,004 \text{ kips}} \\ &= 0.0781 \text{ ft} \end{aligned}$$

$$\begin{aligned} L &= e + L_o \\ &= 0.0781 \text{ ft} + 30.1496 \text{ ft} \\ &= 30.2277 \text{ ft} \end{aligned}$$

5. Find the horizontal reactions using Equation 17:

$$\begin{aligned} F &= \frac{H_o}{\left(\frac{L}{T} + \frac{1}{K_1} + \frac{1}{K_2}\right)} \\ &= \frac{30.0 \text{ ft}}{\left[\left(\frac{30.2277 \text{ ft}}{2.60 \text{ kips}}\right) + \left(\frac{1}{\infty}\right) + \left(\frac{1}{2.00 \text{ kip/ft}}\right)\right]} \\ &= 2.4741 \text{ kips} \end{aligned}$$

6. Find the arresting force using Equation 7:

$$\begin{aligned} P &= 2\sqrt{T^2 - F^2} \\ &= 2\sqrt{(2.60 \text{ kips})^2 - (2.4741 \text{ kips})^2} \\ &= 1.5985 \text{ kips} \end{aligned}$$

7. Find the reduced span using Equation 15:

$$\begin{aligned} H &= H_o - F\left(\frac{1}{K_1} + \frac{1}{K_2}\right) \\ &= 30.0 \text{ ft} - 2.4741 \text{ ft}\left(\frac{1}{\infty} + \frac{1}{2.00 \text{ kip/ft}}\right) \\ &= 28.7629 \text{ ft} \end{aligned}$$

Table 2. Example 2 Results							
<i>T</i> (kips)	<i>F</i> (kips)	<i>P</i> (kips)	<i>L</i> (ft)	<i>H</i> (ft)	<i>S</i> (ft)	<i>U</i> (kip-ft)	<i>W</i> (kip-ft)
2.55	2.428	1.556	30.226	28.786	4.610	1.572	1.584
2.60	2.474	1.599	30.228	28.763	4.648	1.632	1.596
2.65	2.519	1.643	30.229	28.740	4.685	1.692	1.607

8. Find the sag using Equation 9:

$$\begin{aligned}
 S &= \frac{\sqrt{L^2 - H^2}}{2} \\
 &= \frac{\sqrt{(30.2277 \text{ ft})^2 + (28.7629 \text{ ft})^2}}{2} \\
 &= 4.6478 \text{ ft}
 \end{aligned}$$

9. Find the strain energy in the cable and horizontal supports using Equation 10:

$$\begin{aligned}
 U &= \left(\frac{1}{2}\right) \left[ \frac{T^2 L_0}{AE} + F^2 \left( \frac{1}{K_1} + \frac{1}{K_2} \right) \right] \\
 &= \left(\frac{1}{2}\right) \left[ \frac{(2.60 \text{ kips})^2 (30.1496 \text{ ft})}{1,004 \text{ kips}} + (2.4741 \text{ kips})^2 \left( \frac{1}{\infty} + \frac{1}{2.00 \text{ kip/ft}} \right) \right] \\
 &= 1.6318 \text{ kip-ft}
 \end{aligned}$$

10. Find the change in potential energy using Equation 11:

$$\begin{aligned}
 W &= W_0(D_0 + S - S_0) \\
 &= (0.310 \text{ kips})(2.00 \text{ ft} + 4.6478 \text{ ft} - 1.50 \text{ ft}) \\
 &= 1.5958 \text{ kip-ft}
 \end{aligned}$$

11. The energy equation balances within 3%. Other values of *T* may be tried by returning to step 3. The result of trials of nearby values of *T* made with a spreadsheet are summarized in Table 2. The energy equation will balance when *T* is between 2.55 and 2.60 kips. Either of these may be used to check the limit states, or *T* can be computed as precisely as desired by returning to step 3 for further reiteration. Were this to be done, the more precise value of *T* = 2.57 kip would be confirmed.

12. *T* = 2.60 kip will be used to check the limit states.

a. The cable strength is checked:

$$T_n/2 = 7.20 \text{ kips} > T = 2.60 \text{ kips} \quad \text{o.k.}$$

b. The stopping distance is checked:

$$\begin{aligned}
 D_s &= S - S_0 \\
 &= 4.6478 \text{ ft} - 1.50 \text{ ft} \\
 &= 3.1478 \text{ ft} < 3.50 \text{ ft} \quad \text{o.k.}
 \end{aligned}$$

Table 3. (So, Sc) Pairs	
Sc (%)	So (%)
2.60	3.00
3.00	3.47
3.46	4.00
3.50	4.04
4.00	4.62
4.32	5.00
4.50	5.18
5.00	5.77
5.18	6.00
5.50	6.35
6.00	6.90
6.07	7.00
6.50	7.47
6.91	8.00
7.00	8.06
7.50	8.64
7.78	9.00
8.00	9.20
8.50	9.76
8.65	10.00
9.00	10.32
9.50	10.96
9.51	11.00
10.00	11.48
10.39	12.00

c. Free fall is limited by lanyard slack adjustment:

$$D_o = 2.00 \text{ ft} < 6.00 \text{ ft} \quad \mathbf{o.k.}$$

d. The total fall ( $D_o + D_s$ ) must be checked against distance to obstacles:

$$D_o + D_s = 2.00 \text{ ft} + 3.1478 \text{ ft} = 5.1478 \text{ ft}$$

e. The arresting force is checked:

$$P = 1.5990 \text{ kip} = 1,599 \text{ lb} < 1,800 \text{ lb} \quad \mathbf{o.k.}$$

When compared with Example 1, the arresting force has been reduced to an acceptable level by the elasticity of the horizontal support and reduction of initial sag. Tension in the HLL and the loads on its anchors are also significantly reduced.

### Specifying Initial Sag in the HLL

As mentioned in the “Design Overview,” the initial sag in the unloaded HLL will be a catenary. If the designer chooses to specify catenary sag, it only remains to relate the sag,  $S_c$ , of the unloaded catenary to the initial V-shaped sag,  $S_o$ , when the slack is first taken up during a fall. The length of the cable can be found from the span  $H_o$  and sag  $S_o$ , and then the catenary sag,  $S_c$ , can be calculated.

Results of calculating ( $S_o$ ,  $S_c$ ) pairs to two decimal places of precision are given in Table 3. From Table 1, the initial V-shaped sags  $S_o$  of 10% and 5% in the preceding examples correspond to catenary sags  $S_c$  of 8.65% and 4.32%, respectively, at time of installation. An approximate linearized expression may also be used.

$$S_c = 0.864S_o \quad (18)$$

For these same values of V-shaped sag  $S_o$ , Equation 18 gives catenary sag  $S_c$  of 8.64% and 4.32%, respectively.

### CONCLUSION

A method of calculating the arresting force by rational analysis and comparing the state of the PFAS with the limit states of the system has been presented herein. Conservation of energy is tested for trial values of HLLs with cable tension  $T$ . Having identified the correct value of cable tension to any desired precision by reiterative analysis, the maximum arresting force and other items of interest can be compared with the limit states. When the results are unsatisfactory, changing the selection of cable, changing the initial sag, introducing a spring in the HLL or introducing elasticity in the horizontal supports are among the many available remedies. Examples and suggestions for analysis of modifications are given in this paper.

The energy absorbed within the body of a person has not been accounted for. The assumptions that no energy is dissipated by the PFAS, that lanyards and supports are very stiff, and that the falling object is a point mass all act to stiffen the system and increase the arresting force. Ignoring the inertia within the PFAS (e.g., inertia of an elastic support) acts to soften the system and decrease the arresting force. In the absence of damping, a PFAS would be oscillatory, but in every real PFAS, there will be many sources of damping whereby energy is absorbed and dissipated. Suggestions that a good estimate of the arresting force is two times the weight of a person are known from field tests to be inaccurate in the general case.

### SYMBOLS

$AE$	HLL cable property = Metallic area times the effective modulus of elasticity, kips
$Do$	Free-fall distance, same as slack in PFAS lanyard, ft
$F$	Horizontal reaction at support, kips
$H$	Horizontal span after displacement of supports under load, ft
$H_o$	Initial span of HLL, ft
$K_1, K_2$	Stiffness of horizontal supports, kip/ft
$Ke$	Effective stiffness of the HLL, kip/ft
$Ks$	Stiffness of a spring included in a HLL, kip/ft
$L$	Total length of cable under load, ft
$Lo$	Initial length of unloaded cable, ft
$P$	Arresting force applied to cable, kip
$R$	Vertical reaction at support, kip
$S$	Sag of cable in the V configuration under load, ft
$S_c$	Initial sag at rest in a catenary configuration, ft
$S_o$	Initial V-shaped sag at rest, ft
$T$	Tension in the HLL cable, kip
$Tn$	Cable breaking strength, kip
$U$	Strain energy, ft-kip
$W$	External work = Change in potential energy, ft-kip
$Wo$	Weight of a falling person with equipment, kip
$e$	Elongation of cable under load $T$ , ft

### REFERENCES

- ACCT (2012), *ACCT Standards*, 8th ed., The Association for Challenge Course Technology, Deerfield, IL, Appendix A, p. 70.
- ASTM (2009), *Standard Specification for Stranded Carbon Steel Wire Ropes for General Purposes*, ASTM A1023/A1023M—09e1, ASTM International, West Conshohocken, PA.
- ASTM (2013), *Standard Test Method for Tension Testing of Wire Ropes and Strand*, A931-08, ASTM International, West Conshohocken, PA.
- ASTM (2014a), *Standard Specification for Zinc-Coated Steel Structural Wire Rope*, A603-98, ASTM International, West Conshohocken, PA.

- ASTM (2014b), *Standard Specification for Zinc-Coated Parallel and Helical Steel Wire Structural Strand*, A586-04, ASTM International, West Conshohocken, PA.
- GSA (2007), *Wire Rope and Strand*, Federal Specifications Standard RR-W-410E, General Services Administration, Washington, DC.
- Jacobs, Keith, private correspondence, November 17, 2014, with the author, Experiential Systems, Lansing IL.
- OSHA (n.d. a), *Code of Federal Regulations Title 29, Part 1926—Safety and Health Regulations for Construction*; Standard 1926.32—Definitions; Standard 1926.104—Safety belts, lifelines, and lanyards; Standard 1926.502—Fall protection systems criteria and practices; Occupational Safety and Health Administration, <https://www.osha.gov/law-regs.html>, accessed May 18, 2015.
- OSHA (n.d. b), *Construction eTool, Construction Home, Glossary, General Construction*, Occupational Safety and Health Administration, <https://www.osha.gov/SLTC/etools/construction/glossary.html>, accessed May 19, 2015.
- OSHAcademy (n.d.), *Personal Fall-Arrest Systems*, Tab 5.7, Geigle Safety Group, Inc., Beaverton OR, <http://www.oshatrain.org/courses/mods/714m5.html>, accessed May 18, 2015.
- State of Illinois (1989), *Structural Engineering Practice Act of 1989*, 225 ILCS 340/5, Springfield, IL.

# Tensile Strength of Embedded Anchor Groups: Tests and Strength Models

DAVID A. GRILLI and AMIT M. KANVINDE

---

## ABSTRACT

Steel column bases in seismically braced frames and other similar structures must be designed for high uplift or tensile forces. A common detail for this connection involves anchors embedded in the footing with a plate at their lower end, also embedded in the footing. This detail is increasingly prevalent in construction practice because it is exempt from the strength calculations of ACI 318 Appendix D. However, no experimental data or validated design guidelines are available to support the design of this detail. As a consequence, approaches from other similar situations (such as punching shear of slabs) are adapted for this purpose. To address this practical need, this paper presents tension tests on two full-scale specimens featuring this anchorage detail. The main variable examined in the experiments is the embedment depth, such that two depths (12 and 18 in.) are tested. The test specimens exhibit a classic concrete failure cone extending upward from the edges of the embedded base plate. The experimental data provide evidence that the anchorage detail provides an effective means to carry high-tensile loads. The data are evaluated against three strength models, including the ACI 318 Appendix D method, the ACI 318 punching shear equation and the concrete capacity design (CCD) method. It is determined that the ACI 318 Appendix D method is significantly conservative (average test-predicted ratio of 1.34) because it does not consider the beneficial effects of the embedded plate. On the other hand, the punching shear method has an average test-predicted ratio of 0.62. The CCD method shows the most promise, with an average test-predicted ratio of 0.99. Limitations of the study include the small size of the test set and the minimal reinforcement in the specimens.

**Keywords:** anchorages; base connections.

---

## INTRODUCTION

Column bases in steel frames (particularly braced frames) must often be designed for high-tensile (i.e., uplift) forces. These forces may be a result of overturning moments induced by high-seismic or -wind events or, in the case of concentrically based frames, for the development of the tensile capacity of diagonal braces as required by current steel design provisions (AISC, 2010). Various detailing alternatives are available for transferring this tensile force from the steel column into the concrete footing below. Figures 1a and b show two such details that are commonly used in current construction practice.

Figure 1a shows a detail that uses individual, standard-headed anchors or anchor rods with nuts at the embedded ends. While convenient to fabricate, these details are problematic if large tensile loads (i.e., >50 kips or so) must be resisted for the following reasons: (1) The strength is

calculated in accordance with ACI 318-14 Appendix D (ACI, 2014) as the group capacity based on individual, standard-headed anchor bolts or nutted anchor rods. In many cases, the embedment depth or number of anchor rods required by this provision becomes impractical. (2) There is an apparent dichotomy wherein the strength calculation of a similar detail for reinforced concrete columns with hooked reinforcement bars extending into the footing is not subject to ACI 318 Appendix D requirements; only the rebar tensile strength is checked. This results in strength estimates that are significantly higher than those determined as per ACI 318 Appendix D.

In response to these issues, designers often employ a detail similar to that shown in Figure 1b. This detail resists uplift force through a single plate embedded at the lower end of the anchor bolts. This detail will typically include supplemental reinforcement around the embedded plate. This detail is attractive to designers because the provisions of ACI 318 Appendix D explicitly state that such a detail is outside its scope. Specifically, referring to ACI 318 D.2.2:

Specialty inserts, through-bolts, multiple anchors connected to a single steel plate at the embedded end of the anchors, grouted anchors, and direct anchors such as powder or pneumatic actuated nails or bolts are not included in the provisions of Appendix D.

The detail shown in Figure 1b circumvents the provisions of Appendix D. However, Appendix D (or any other design

---

David A. Grilli, Graduate Research Assistant, Department of Civil and Environmental Engineering, University of California, Davis, CA. Email: [dagrilli@ucdavis.edu](mailto:dagrilli@ucdavis.edu)

Amit M. Kanvinde, Professor, Department of Civil and Environmental Engineering, University of California, Davis, CA (corresponding). Email: [kanvinde@ucdavis.edu](mailto:kanvinde@ucdavis.edu)

---

standard) does not provide a method for the design of such a detail, with the implication that either engineering judgment must be used or alternative design provisions must be adapted for design. These alternatives include the current ACI provisions for punching shear (ACI 318, Chapter 11) or bearing capacity (ACI 318, Chapter 10) of concrete members. At first glance, these situations (i.e., the embedded plate details and punching shear/bearing) appear similar. However, there are subtle differences in physical response between these situations and the anchorage details such as the one shown in Figure 1b. Specifically, these pertain to (1) the reinforcing of the footing with respect to the embedded plate, (2) installation of the embedded plate itself (i.e., if the embedded plate needs to be cast in a protective lean mix below the bottom of footing prior to the footing pour, such that the plate is actually bearing against a cast surface rather than cast within the footing) and (3) size effects in concrete (i.e., the embedment of these connections is often larger than seen in slab/punching shear situations, and thus these may be weaker on a unit basis as compared to situations for which the punching shear approaches have been developed). In the absence of guidance for the design of these anchorages in ACI 318 or any other design codes and the absence of test data that demonstrate their strength and response, engineers and review agencies are often required to make design choices that are expensive and possibly conservative (e.g., requiring the plate to be positioned such that it bears on the bottom of the concrete footing).

Motivated by these problems, this paper presents results on two full-scale tests on anchorage details similar to the ones shown in Figure 1b. The primary objectives of this study are as follows:

1. To develop fundamental understanding of the failure modes and force transfer mechanisms in anchor group details subjected to tension uplift, based on large-/full-scale experimental data.

2. To develop, validate and establish design provisions for these details that are otherwise specifically excluded from ACI 318 Appendix D.
3. To demonstrate details that can economically achieve design strength for high uplift forces.

This paper describes two full-scale experiments conducted to accomplish these objectives. The next section describes the experiments and presents their results relative to commonly used strength prediction models. The paper concludes by summarizing possible design methods.

## EXPERIMENTAL PROGRAM

Two large-scale experiments were conducted to realize the objectives of the study. The primary variable considered was the embedment depth,  $d_{embed}$ , indicated schematically in Figure 1b. In this study, two embedment depths were considered—that is,  $d_{embed} = 12$  and 18 in. Figure 2 shows a photograph of the test setup and specimen prior to testing, whereas Figure 3 schematically shows various detailing/reinforcement aspects of the specimens. The photograph in Figure 2 shows test 1; the test specimen for test 2 appears identical—the only difference is in the embedment depth.

### Test Setup

Referring to Figures 2 and 3, the key aspects of the test setup are as follows:

1. Both specimens featured blocks that measured 40 in. (height)  $\times$  140 in.  $\times$  108 in. The large size of the block was necessitated by the following considerations:

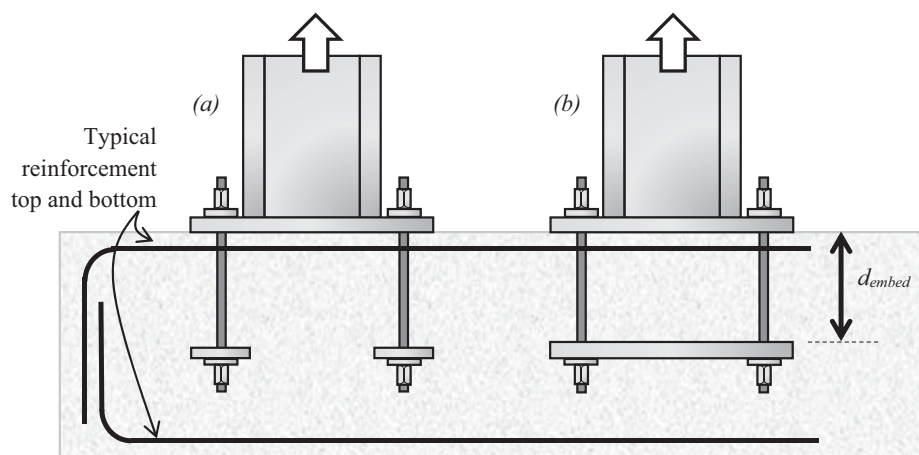


Fig. 1. (a) Base connection with individual anchors; (b) base connection with anchors connected to an embedded plate.

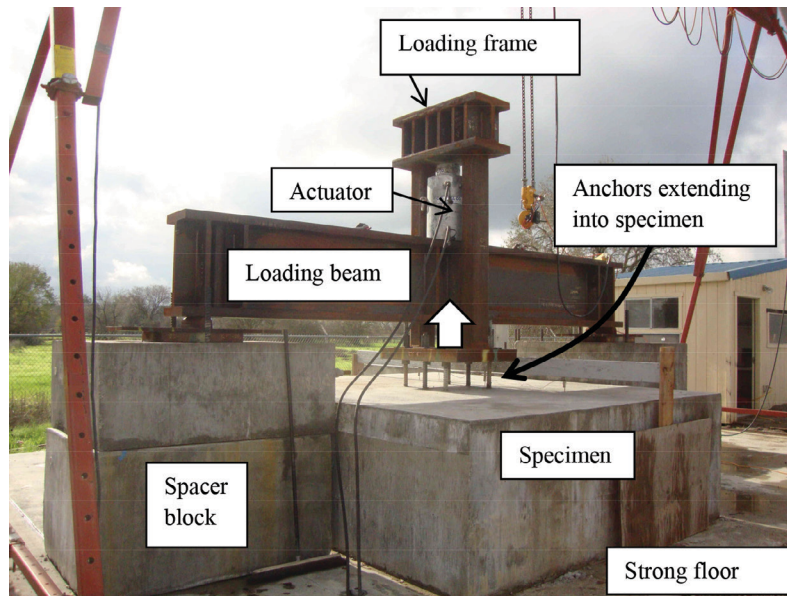


Fig. 2. Photograph of test setup.

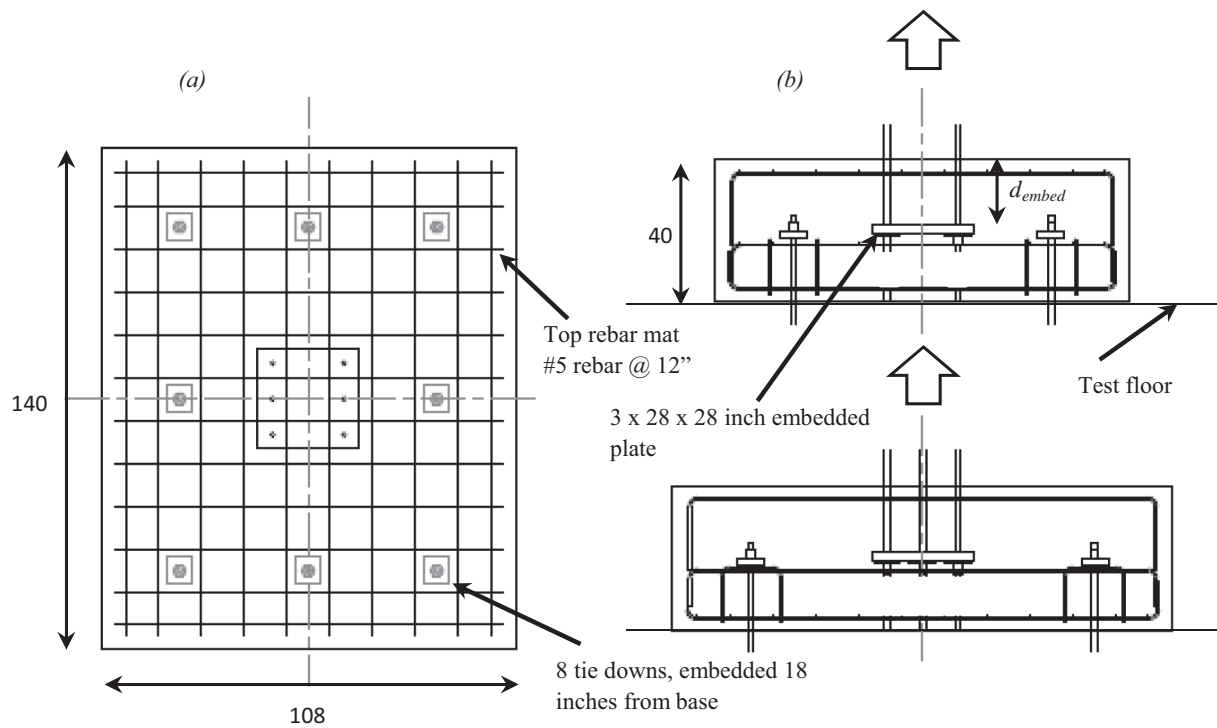


Fig. 3. Specimen details: (a) plan; (b) two elevations.

- a. In plan, the large dimension was necessary to ensure that the failure cone was fully accommodated within the footing, thereby avoiding edge effects. In fact, the size of the block was large enough that the zones of compressive stress induced by the tie-down rods (shown in Figure 3b) had minimal effect on the possible failure cone.
  - b. In elevation, a key consideration was to ensure that the underside of the specimen (i.e., below the applied load) was anchored to the strong floor such that failure of the footing did not occur due to bending. An especially important consideration here is that experimental strength for pure tensile failure is relatively unaffected by boundary conditions.
2. Following from point 1, the anchor system was elaborately designed with two considerations, with competing effects: (a) spacing the outside anchors as far out as possible to minimize interaction with the failure cone and (b) including anchors in the line of action of the loads to preclude bending of the block. This latter consideration was realized by installing tie-downs projecting upward from the strong floor over which the specimen was cast in place. These tie-downs (whose locations are shown in Figure 3) had an embedded plate attached to their top surface to enable engagement with the specimen.
  3. The loading apparatus, as shown in Figure 2, included a cross beam and a frame between which a hydraulic cylinder actuator (with 1,000-kip capacity) was inserted such that the loading frame could be lifted up. A 4-in. plate was attached to the lower surface of the loading frame. Six anchor rods attached to this plate were embedded in the concrete and attached to the embedded plate, which in turn exerted the uplift forces on the concrete. The embedded plates were identical in both test specimens, and measured 3 in.  $\times$  28 in.  $\times$  28 in. (the plate was sized to remain elastic under the applied loads). The anchor rods were A722 Grade 150 rods of 1 $\frac{3}{8}$ -in. diameter and designed to remain elastic during the loading.
  4. Reinforcement was provided in the top layer. This consisted of a light rebar mat, which consisted of #5 rebar with a spacing of 12 in. The reinforcement was used to provide minor resistance against uplift as well as to mitigate surface cracking. No vertical reinforcement was provided. The main purpose of this was to isolate the effect of the concrete resistance in a clean way such that it would be transferable to design situations with varying reinforcement wherein

the contribution of reinforcement is addressed separately. A systematic study of the effect of reinforcement is possible through additional testing, which varies the reinforcement as a test parameter.

5. Both specimens were cast on the same day, although tested on different days. Test 1 was tested on day 28 with respect to the pour, whereas test 2 was tested on day 31. Standard test cylinders were taken from each of these pours to measure the compressive strength of concrete  $f'_c$ ; results from these ancillary tests are presented in a subsequent section.
6. The specimens were all loaded monotonically, with an approximate rate of 1 kip per second.

### Test Instrumentation

The load in the specimens was monitored using a pressure gage. As a secondary measurement of load, a linear strain gage was attached to the top surface of the loading beam, which remained elastic throughout the loading. Displacement transducers were affixed to three locations on the top surface of the concrete as well as to the top plate to measure upward displacement of the loading frame. A camera was suspended directly above the test setup to capture crack formation in the entire block. Another camera captured an elevation (profile) view of the test to observe vertical displacements of the test equipment and concrete failure cone. Based on these instruments, a load deformation curve was generated, results of which are discussed in a subsequent section.

### Ancillary Tests

Six standard, 6-in.  $\times$  12-in. concrete cylinder samples were collected and tested at the 28-day cure mark. For the construction of the specimen blocks, a total of three trucks were required, and two samples from each truck were tested. The analysis of test data relative to the models (discussed in a subsequent section) is based on the average value of  $f'_c = 4,336$  psi (standard deviation of 282 psi) for the cylinder samples for each test. The low standard deviation suggests a relatively uniform strength throughout the specimen block. The weight density of the various samples was (on average) 145 lb/ft<sup>3</sup>, which is consistent with plain structural concrete used in practice.

### Test Results

Load-displacement curves for both experiments are shown in Figure 4. Peak loads (denoted  $P_{test}^{max}$  and also shown on the figure) are summarized in Table 1. Both tests showed similar response, wherein little physical damage was observable in the initial elastic region of loading. Failure was observed

**Table 1. Test Results and Comparison with Strength Prediction Methods**

$d_{embed}$ (in.)	$P_{test}^{max}$ (kips)	Test-to-Predicted Ratios		
		$P_{test}^{max} / P_n^{ACI318-D}$	$P_{test}^{max} / P_n^{PS}$	$P_{test}^{max} / P_n^{CCD}$
12	317	1.29 (1.58)*	0.65	0.92 (1.13)†
18	495	1.39 (1.61)*	0.59	1.07 (1.21)†
<b>Mean</b>		1.34 (1.60)*	0.62	0.99 (1.17)†
<b>Coefficient of Variation</b>		0.05 (0.01)*	0.07	0.11 (0.05)†

\* Value in parentheses calculated without considering increase in perimeter of projected area due to plate thickness as allowed by (ACI 318, D.5.2.8).  
 † Value in parentheses calculated by excluding area of plate from projected area.

in the form of (1) a sudden drop in load, (2) appearance of a crack on the top surface of the concrete, and (3) a lifting of the “failure cone” by approximately 2 in. The failure of test 2, with  $d_{embed} = 18$  in., was somewhat more sudden as compared to that of test 1. Other than the concrete failure, all components in the setup (i.e., anchors, embedded plate, loading beam) remained elastic as designed.

Figures 5a and b show post-test photographs of tests 1 and 2 taken from a high angle above the specimens, illustrating the entire failure surface after the loading beam had been removed. Figures 6a and b show similar profile photographs, illustrating the uplift of the concrete cone. Based on the location of this crack, an inferred profile of the failure cone is illustrated schematically in Figures 7a and b. Referring to the figures and physical measurements of the failure cone, the approximate angle of the failure cone surface with respect to the horizontal is  $28^\circ$  for test 1 and  $33^\circ$  for test 2.

**STRENGTH MODELS**

Referring to the introductory discussion, a major objective of this paper is to provide support for the development of

strength characterization approaches for these anchorages. Accordingly, three strength characterization approaches are evaluated against the test data. These are (1) the ACI 318 Appendix D approach for the breakout strength of anchor groups, (2) the ACI 318 Chapter 11 punching shear equation and (3) the concrete capacity design (CCD) approach proposed by Fuchs et al. (1995). The first two are selected based on their prevalence in design practice, whereas the third is selected based on its promise in characterizing the strength of a large variety of concrete embedments and fastenings, as shown by previous studies (e.g., Gomez et al., 2009). Each of these methods is now briefly described, and the resulting strength estimates are compared to test data.

**Method 1**

ACI 318 Appendix D provides the following equation (which has been adapted to the current test parameters) to predict the breakout strength of an anchor group in concrete (loaded concentrically, cast-in anchors, no edge effects):

$$P_n^{ACI318-D} = \frac{A_{Nc}}{A_{Nco}} \times \psi_{c,N} \times N_b \tag{1}$$

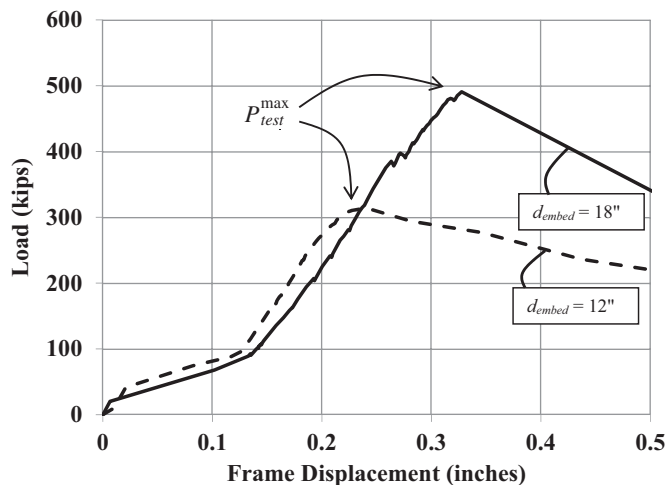


Fig. 4. Load deformation curves of the two specimens.



Fig. 5. Overhead view of breakout surface: (a) 12-in. embedment; (b) 18-in. embedment.



Fig. 6. Profile view of breakout surface: (a) 12-in. embedment; (b) 18-in. embedment.

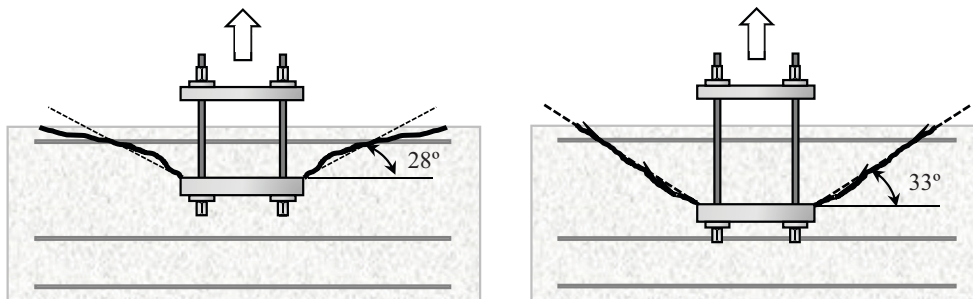


Fig. 7. Schematic illustration of breakout cone: (a) 12-in. embedment; (b) 18-in. embedment.

where, for 11 in.  $< d_{embed} < 23$  in.,

$$N_b = 16 \times \sqrt{f'_c} \times d_{embed} \quad (2)$$

and

$A_{Nc}$  = projected concrete failure area of a group of anchors, in.<sup>2</sup>

$A_{Nco}$  = projected concrete failure area of a single anchor, in.<sup>2</sup>

$\psi_{c,N} = 1.25$  for cast-in anchors without cracking at service loads

This method was derived based on both the tensile capacity of concrete and fracture mechanics concepts. The projected area is defined by projecting planes from the anchorage depth to the free surface at 35° angles. Modification factors are used when the planes intersect free-side surfaces. This method is based on experimental data on embedded single anchors and anchor groups (Klingner et al., 1982; Cook and Klingner, 1992; Fuchs et al., 1995; Farrow and Klingner, 1995; Zhang et al., 2001; Anderson and Meinheit, 2005; Eligehausen et al., 2006; Lee et al., 2007; Ožbolt et al., 2007) and, as a result, is accurate for deeply embedded single anchors and anchor groups. For the same reason, this approach cannot account for the favorable effects of connecting the embedded anchors to a common plate. In fact, the strength estimate implied by Equation 1 is identical to the calculations that would result from considering the anchor group without a plate present. It may be argued that this is conservative because it does not account for (1) the larger bearing area of the concrete that may delay fracture initiation and (2) a greater degree of confinement in the concrete above the plate. While the method does not explicitly account for the plate as a bearing surface, the plate may be considered effective as a washer to determine the location from which the failure surface originates (per provision D.5.2.8 of the Appendix). Per this provision, the effective dimension of this plate or washer may be considered equal to the thickness of the attached plate (3 in. in this case).

## Method 2

ACI 318 Chapter 11 provides provisions for punching shear to be used in the case where a column exerts a vertical load on a reinforced concrete slab. As discussed in the introductory remarks, this method is sometimes used for anchorage design because the modes of failure appear to be similar. Using this approach, the applicable equation is

$$P_n^{PS} = 4 \times \sqrt{f'_c} \times b_0 \times d_{embed} \quad (3)$$

The equations have been greatly simplified for ease of design and are based on fitting to experimental data (ACI-ASCE, 1962). Strength predictions are based on the depth

of the slab, concrete material properties and a “critical section” based on the loading area and depth of the slab. The formulation is intended to reduce the dependency of strength on ratio of column size to slab depth. The critical section is defined as the area that minimizes the perimeter a minimum while maintaining a distance of  $d_{embed}/2$  to the edges or corners of the column or loading area. This may be interpreted to imply that failure occurs when a tensile stress of  $4 \times \sqrt{f'_c}$  is reached over the projected area of a 45° failure cone emanating from the edges of the embedded plate. For the particular geometry of the specimens used in this study,  $b_0$  may be calculated using the following equation:

$$b_0 = 4 (28 \text{ in.} + d_{embed}) \quad (4)$$

However, a closer inspection of the sources (ACI-ASCE, 1962) used to formulate this approach reveal two interesting factors. First, it does not explicitly incorporate fracture mechanics or the “size effect” in concrete (Bažant, 1984), which implies that the unit strength (or failure stress) of geometrically self-similar concrete components varies inversely with their size because failure is controlled by localized fracture rather than by large-scale yielding. The presence of reinforcement mitigates this effect by distributing deformations. Second, this equation is based on 198 tests on concrete slabs that were reinforced and included a large set of data on slabs thinner than 10 to 12 in. When considered together, these two points present an obvious challenge in extrapolating the equation to the anchorages tested, which have significantly deeper embedment and are also dissimilar physically as compared to a concrete column on a slab.

## Method 3

Another approach, which explicitly considers the size effect, is based on a method originally proposed Fuchs et al., (1995). This method, referred to as the concrete capacity design (CCD) method has been demonstrated to characterize concrete failure strength for a wide variety of fastenings, including shear lugs (Gomez et al., 2009). In fact, the method used in ACI-318 Appendix D is partially based on the CCD method. The nominal breakout capacity of concrete for cast-in anchors as derived in the CCD method, adapted to the conditions of the tests, can be reduced to the following equation:

$$P_n^{CCD} = \frac{1}{\sqrt{d_{embed}}} \times \left( \frac{40}{9} \right) \times \sqrt{f'_c} \times A_{Nc} \quad (5)$$

where  $A_{Nc}$  refers to the projected area assuming a 35° breakout cone, shown schematically in Figure 8.

Referring to Equation 5, the term  $\sqrt{d_{embed}}$  in the denominator of the right-hand side of the equation may be interpreted as a modifier that explicitly incorporates the size effect such that the effective tensile stress capacity (or unit

strength) of the concrete is diminished as the embedment depth increases. The square root dependence of the effective stress may be determined directly from fracture mechanics concepts (Anderson, 1995). Another observation is that the area  $A_{Nc}$  is different as compared to the area used in the punching shear method (in Equation 3). However, as identified previously (Gomez et al., 2009), the projected area does not bear physical significance to the final breakout surface, which is a result of fracture propagation, but rather may be interpreted as a convenient basis for characterizing the effective stress at which fracture initiation occurs. The projected area may be calculated in two ways—one includes the area of the embedded plate within it, whereas the other excludes it. Inclusion of the area of the embedded plate assumes that the adhesive bond developed between the underside of the plate and the concrete is greater than the concrete tensile strength, whereas the exclusion assumes that no adhesion is present. The effect of these assumptions is discussed in the next section.

## DISCUSSION

Test-predicted ratios for the three models are presented in Table 1. Referring to the table, the following observations may be made:

1. The ACI-318 Appendix D method is quite conservative; the test-predicted ratios  $P_{test}^{max} / P_n^{ACI318-D}$  are determined to be 1.29 and 1.39 for tests 1 and 2, respectively (average of 1.34). This is an important observation, confirming the concerns about the Appendix D method raised earlier, because it provides empirical evidence that the method may not be economical for designing connections with an embedded plate. It is important to note here that the attached plate in these tests is fairly thick (3 in.). As a result, the use of provision D.5.2.8, which allows the consideration of the plate thickness as an effective washer dimension, significantly adds to the strength. If the strength is calculated without considering this

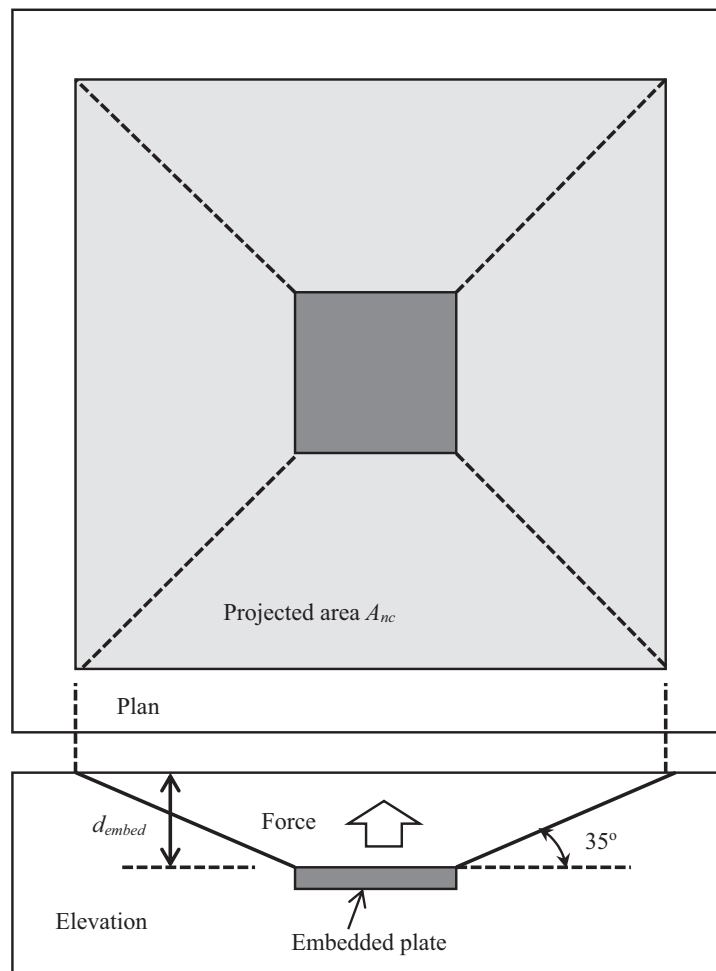


Fig. 8. Effective projected area for CCD method (may or may not include area of plate).

increase in perimeter (i.e., projecting the failure area from the anchor rods), then the conservatism of the ACI method is increased, such that the average test-predicted ratio is 1.60, as indicated in Table 1.

2. For the ACI punching shear method, the test-predicted ratios  $P_{test}^{max}/P_n^{PS}$  are 0.65 and 0.59 for tests 1 and 2, respectively, suggesting that when considered relative to other methods (such as the CCD method discussed next), this method may not be optimal for designing the anchorages. A closer inspection of the scientific basis for the punching shear method indicates that it is based on 198 tests of slabs, of which many are thin, compared to the embedment depth of the anchorages. As a result, this observation is not entirely surprising. On the other hand, it is important to note that (a) the current study includes only two experiments, such that the limited size of the study may compromise its statistical significance, and (b) the anchorages are different than a concrete column on a slab.
3. The CCD method appears to be the most accurate of the three methods considered. The test-predicted ratios  $P_{test}^{max}/P_n^{CCD}$  are 0.92 and 1.07 for tests 1 and 2, respectively, resulting in an average  $P_{test}^{max}/P_n^{CCD}$  value of 0.995. If the area of the plate is excluded from the projected area, the average test-predicted ratio is 1.17, suggesting that significant adhesion may be present between the steel and the concrete. This is consistent with similar results on concrete-steel adhesion by the Federal Highway Administration (FHWA, 2000), through the use of “pull-off” tests that indicate adhesion stresses in the range of 100 to 150 psi, which are greater than the effective tensile stress used in the CCD method.
4. For each of the models, the test-to-predicted ratios are similar for both tests, indicating that the epistemic error introduced by any of the models is not significantly affected by the embedment depth.

It is informative to compare the assumptions underlying the punching shear method and the CCD method because they provide insight into the physical processes controlling failure. Specifically, the punching shear method assumes that the concrete failure strength is directly proportional to the projected area of the 45° cone, with the implication that a uniform tensile stress is mobilized over the failure surface. Research (Bažant, 1984) has shown that this assumption is realistic only when the characteristic specimen dimension (embedment depth in this case) is within 10 to 20 times the aggregate size—that is, approximately 6 to 8 in. For larger components, failure is controlled by fracture mechanics, wherein failure initiates over a smaller area and then

propagates as the failure cone. As a result, the effective failure stress (when considered over a projected area) is lower. The CCD method explicitly captures this effect.

## SUMMARY AND CONCLUSIONS

Two full-scale experiments were conducted to examine the tensile capacity of anchorage details with anchor bolt groups connected by a plate embedded within a concrete footing. The anchorage type examined in this study is commonly used at the base of columns in braced frames where large uplift forces must be resisted. The tests were motivated by the lack of guidance in design standards for such a detail and by the challenges in adapting design methods originally developed for other types of details.

The main variable interrogated in the experiments was the embedment depth, such that two values—12 and 18 in.—were investigated. The specimens were composed of six anchor rods (1 $\frac{3}{8}$ -in. diameter, A722 Grade 150 rods) connected to a 3-in.  $\times$  28-in.  $\times$  28-in. plate embedded within the concrete. The specimens were designed with minimal reinforcement (to isolate the concrete strength) and were sized to minimize the effect of boundary conditions or specimen bending on the pullout strength. Both tests showed a similar mode of failure with a concrete failure cone emanating at approximately 30° from the edges of the embedded plate.

The specimen strengths were evaluated against three strength characterization approaches. It was found that the concrete capacity design (CCD) method developed by Fuchs et al., (1995) provides excellent agreement with test data. On the other hand, the ACI 318 Appendix D method is significantly conservative, presumably because it does not consider the beneficial effects of the embedded plate.

Finally, it is important to recognize the limitations of this study in interpreting its results. The most obvious limitation is test sample size (i.e., two tests), which was controlled by the physical size and expense of these specimens relative to the budgetary constraints. A consequence of this small sample size is that other variables—such as plate shapes and sizes, anchor rod layouts, edge distances or the use of other embedments instead of a plate (e.g., interconnected channels)—were not examined. Another consequence is that in the absence of replicate tests, it is difficult to isolate the inherent variability in experimental data from epistemic bias in the models evaluated against the data. As a result, the test data, in itself, cannot be used to calibrate resistance (i.e.,  $\phi$ ) factors. Moreover, the test specimens did not contain vertical reinforcement. This was a deliberate decision, considering that these experiments are the some of the first of their kind, and intended to establish fundamental, baseline response of the concrete itself. It is anticipated that the presence of reinforcement will increase the strength through two mechanisms: (1) the additional yielding strength provided by

the rebar and (2) the mitigation of the size effect in concrete. An explicit incorporation of these effects will require additional testing, as well as finite element simulation to generalize the results. These are recommended areas for future work.

### ACKNOWLEDGMENTS

The authors are grateful to the Charles Pankow Foundation and the American Institute of Steel Construction for providing major funding for this project. Supplementary funding was provided by graduate fellowships at the University of California–Davis. The Structural Engineers Association of California (SEAOC) supported the proposal to the major funding sponsors. The authors also thank Bill Sluis and Daret Kehlet, technical personnel at UC Davis, for contributing to this project. The authors acknowledge their contributions, as well as those of the Industry Advisory Committee of the project, including Geoff Bomba of Forell Elsesser Engineers, Ryan Kersting of Buehler and Buehler Structural Engineers, and Paul Cordova of Simpson, Gumpertz and Heger. The findings and opinions presented in this paper are solely those of the authors and not of the sponsors or those acknowledged herein.

### SYMBOLS

$A_{Nc}$	Projected concrete failure area of a group of anchors for ACI 318 Appendix D and CCD methods
$A_{Nco}$	Projected concrete failure area of a single anchor for ACI 318 Appendix D method
$b_0$	Effective perimeter for the punching shear approach
$d_{embed}$	Embedment depth; distance from the concrete surface to top surface of the embedded plate
$f'_c$	Compressive strength of concrete
$P_{test}^{max}$	Maximum load determined from experiment
$P_n^{ACI318-D}$	Strength estimated as per ACI 318 Appendix D
$P_n^{CCD}$	Strength estimated as per the CCD approach
$P_n^{PS}$	Punching shear strength estimated as per ACI 318 Chapter 11
$\Psi_{c,N}$	1.25 for cast-in anchors without cracking at service loads for ACI 318 Appendix D method

### REFERENCES

- ACI (2014), *Building Code Requirements for Structural Concrete and Commentary*, ACI 318-14 and ACI 318R-14, American Concrete Institute, Farmington Hills, MI.
- ACI-ASCE (1962), “Shear and Diagonal Tension,” *ACI Journal, Proc.* Vol. 59, No. 1, Jan., pp. 1–30; No. 2, Feb., pp. 277–334; and No. 3, Mar., pp. 352–396.
- AISC (2010), *Seismic Provisions for Structural Steel Buildings*, AISC 341, American Institute of Steel Construction, Chicago, IL.
- Anderson, N.S. and Meinheit, D.F. (2005), “Pryout Capacity of Cast-In Headed Stud Anchors,” *PCI Journal*, Vol. 50, No. 2, pp. 90–112.
- Anderson, T.L. (1995), *Fracture Mechanics: Fundamentals and Applications*, 2nd ed., Boca Raton, FL: CRC Press.
- Bažant, Z.P. (1984), “Size Effect in Blunt Fracture: Concrete, Rock, Metal,” *Journal of Engineering Mechanics*, ASCE, Vol. 110, No. 4, pp. 518–535.
- Cook, R.A. and Klingner, R.E. (1992), “Behavior of Ductile Multiple-Anchor Steel-to-Concrete Connections with Surface-Mounted Baseplates,” *Anchors in Concrete: Design and Behavior*, SP-130, pp. 61–122, American Concrete Institute, Farmington Hills, MI.
- Eligehausen, R., Mallée, R. and Silva, J. (2006), *Anchorage in Concrete Construction*, Berlin: Ernst & Sohn (J. T. Wiley).
- Farrow, C.B., and Klingner, R.E. (1995), “Tensile Capacity of Anchors with Partial or Overlapping Failure Surfaces: Evaluation of Existing Formulas on an LRFD Basis,” *ACI Structural Journal*, Vol. 92, No. 6, pp. 698–710.
- Federal Highway Administration (2000), “Tensile Bond Strength of a High Performance Concrete Bridge Deck Overlay,” FHWA Project #9904, Project Report, Washington, DC: U.S. Department of Transportation.
- Fuchs, W., Eligehausen, R. and Breen, J.E. (1995), “Concrete Capacity Design (CCD) Approach for Fastening to Concrete,” *ACI Structural Journal*, Vol. 92, No. 1, pp. 73–94.
- Gomez, I.R., Kanvinde, A.M., Smith, C. and Deierlein, G.G. (2009), “Shear Transfer in Exposed Column Base Plates,” Technical Report submitted to the American Institute of Steel Construction, Chicago, IL.
- Klingner, R.E., Mendonca, J.A. and Malik, J.B. (1982), “Effect of Reinforcing Details on the Shear Resistance of Anchor Bolts Under Reversed Cyclic Loading,” *Journal of American Concrete Institute*, Vol. 79, No. 1, pp. 3–12.
- Lee, N.H., Kim, K.S., Bang, C.J. and Park, K.R. (2007), “Tensile-Headed Anchors with Large Diameter and Deep Embedment in Concrete,” *ACI Structural Journal*, Vol. 104, No. 4, pp. 479–486.

Ožbolt, J., Eligehausen, R., Periškić, G. and Mayer, U. (2007), "3D FE Analysis of Anchor Bolts with Large Embedment Depths," *Engineering Fracture Mechanics*, Vol. 74, pp. 168–178.

Zhang, Y.G., Klingner, R.E. and Graves, H.L. (2001), "Seismic Response of Multiple-Anchor Connections to Concrete," *ACI Structural Journal*, Vol. 98, No. 6, pp. 811–822.



# Cross-Section Strength of Circular Concrete-Filled Steel Tube Beam-Columns

MARK D. DENAVIT, JEROME F. HAJJAR and ROBERTO T. LEON

## ABSTRACT

Closed-form expressions for the cross-section strength of steel-concrete composite beam-columns according to the plastic stress distribution method are tabulated in the AISC *Seismic Design Manual* and the AISC *Design Examples*. Approximations have been used in the derivation of these formulas, most of which do not significantly affect the accuracy of the results. However, an approximation in the equation for the axial strength of circular, concrete-filled steel tubes that are simultaneously subjected to flexure at one of the key points on the interaction curve (designated as Point E) leads to results that are unconservative. The derivation of the equation is reviewed and a more accurate expression is proposed.

**Keywords:** steel-concrete composite, concrete-filled steel tube, beam-column strength, cross-section strength.

## INTRODUCTION

The AISC *Specification for Structural Steel Buildings* (2010) allows for the cross-section strength of compact composite columns to be computed by the plastic stress distribution method. In this method, the steel components are assumed to have reached the yield stress,  $F_y$ , in either tension or compression, and the concrete components are assumed to have reached a stress of  $0.85f'_c$  in compression, where  $f'_c$  is the concrete compressive strength. A higher stress,  $0.95f'_c$ , is permitted for circular, concrete-filled steel tubes to account for confinement. As a design aid, closed-form expressions defining several anchor points, labeled Points A through E on the interaction diagram (Figure 1), are tabulated in the AISC *Seismic Design Manual* (AISC, 2012) and the AISC *Design Examples* (AISC, 2011). Approximations were made in the derivation of some of the closed-form expressions, typically resulting in negligible variation from the exact solution. In this case, “exact” refers to axial load and bending moment pairs that have been precisely calculated from the assumed plastic stress distribution and assumed cross-sectional geometry. However, the equation for the axial

strength of circular concrete-filled steel tubes at Point E (Equation 4) tabulated in the AISC publications (2011, 2012) produces results that are unconservative due to an assumption made in its derivation.

## DERIVATION

Point E is defined by a plastic neutral axis location a distance  $h_E$  from the centroid, where  $h_E$  is the average of  $h_n$ , the location of the plastic neutral axis for pure bending (Point B) and the distance to the inside face of the steel tube. The assumed stress distribution at Point E is shown in Figure 2. Based on this stress distribution, the axial compression,  $P_E$ , is defined by Equation 1:

$$P_E = F_y A_{sc} - F_y A_{st} + 0.95 f'_c A_{cc} \quad (1)$$

where

$A_{cc}$  = area of concrete in compression, in.<sup>2</sup>

$A_{sc}$  = area of steel in compression, in.<sup>2</sup>

$A_{st}$  = area of steel in tension, in.<sup>2</sup>

The equation can be revised to relate  $P_E$  to the axial strength under pure compression,  $P_A$ :

$$P_A = F_y A_s + 0.95 f'_c A_c \quad (2)$$

$$P_E = P_A - 2F_y A_{st} - 0.95 f'_c A_{ct} \quad (3)$$

where

$A_c$  = total area of concrete, in.<sup>2</sup>

$A_s$  = total area of steel, in.<sup>2</sup>

$A_{ct}$  = area of concrete in tension, in.<sup>2</sup>

---

Mark D. Denavit, Design Engineer, Stanley D. Lindsey and Associates, Ltd., Atlanta, GA (corresponding). Email: mdenavit@sdlal.com

Jerome F. Hajjar, CDM Smith Professor and Chair, Department of Civil and Environmental Engineering, Northeastern University, Boston, MA. Email: jf.hajjar@neu.edu

Roberto T. Leon, David H. Burrows Professor, Department of Civil and Environmental Engineering, Virginia Tech, Blacksburg, VA. Email: rleon@vt.edu

The current formula for  $P_E$  from Table 7-11B of the AISC *Seismic Manual* is as follows:

$$P_E = P_A - \frac{1}{4} \left[ F_y (d^2 - h^2) + \frac{0.95 f'_c}{2} h^2 \right] (\theta_2 - \sin \theta_2) \quad (4)$$

where

$d$  = outside diameter of steel tube, in.

$h$  = inside diameter of steel tube, in.

The angle between two lines extending from the center of the cross-section to the intersections of the plastic neutral axis and the inside face of the steel tube is calculated as follows (see Figure 2):

$$\theta_2 = \pi - 2 \arcsin \left( \frac{2h_E}{h} \right) \quad (5)$$

Through an examination of Equations 3 and 4, the assumed area of concrete in tension and area of steel in tension can be deduced as Equations 6 and 7, respectively:

$$A_{ct} = \frac{h^2}{8} (\theta_2 - \sin \theta_2) \quad (6)$$

$$A_{st} = \frac{d^2 - h^2}{8} (\theta_2 - \sin \theta_2) = \frac{d^2}{8} (\theta_2 - \sin \theta_2) - A_{ct} \quad (7)$$

Both  $A_{ct}$  and  $A_{st}$  (Equations 6 and 7) are based on circular segment geometry as shown in Figures 3a and 3c. The expression for  $A_{ct}$  exactly represents the shape of the cross-section and given stress pattern; however, the use of  $\theta_2$  for the circular segment in the expression for  $A_{st}$  leads to

an underestimation of the area of steel in tension and thus an overestimation of  $P_E$ . An exact expression for  $A_{st}$  would make use of circular segment geometry with  $\theta_{2s}$  in lieu of  $\theta_2$  (Equations 8 and 9) as shown in Figure 3b:

$$A_{st} = \frac{d^2}{8} (\theta_{2s} - \sin \theta_{2s}) - A_{ct} \quad (8)$$

$$\theta_{2s} = \pi - 2 \arcsin \left( \frac{2h_E}{d} \right) \quad (9)$$

Alternatively, an approximation that is more accurate than the current formula and does not increase the complexity of the calculation by introducing a second angle can be obtained by assuming a circular-sector geometry (Figure 3d), where  $A_{st}$  is computed by Equation 10. Most importantly, the circular-sector geometry matches the geometric assumption used in the formula for the bending moment at Point E,  $M_E$  (Geschwindner, 2010). The final formula for  $P_E$ , using Equation 10 for the area of steel in tension, is Equation 11. This expression is recommended to replace the current formula (Equation 4) in the design tables.

$$A_{st} = \frac{d^2 - h^2}{8} \theta_2 \quad (10)$$

$$P_E = P_A - \frac{1}{4} F_y (d^2 - h^2) \theta_2 - \frac{1}{8} 0.95 f'_c h^2 (\theta_2 - \sin \theta_2) \quad (11)$$

An example illustrating the accuracy of the proposed equation is presented in the following section.

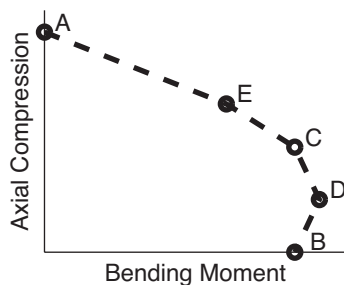


Fig. 1. Schematic interaction diagram.

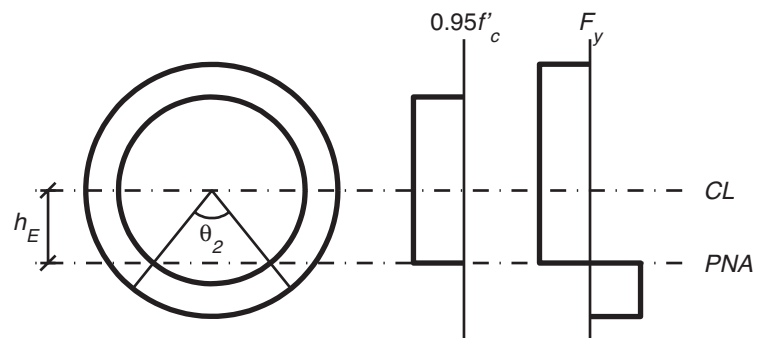


Fig. 2. Assumed stress distribution.

## DESIGN EXAMPLE

**Given:**

Determine the axial compression and bending moment at Point E for an ASTM A500 Grade C HSS10.750×0.250 composite compression member filled with 5-ksi concrete ( $f'_c = 5$  ksi).

From AISC *Manual* Table 2-4, the material properties are as follows:

ASTM A500 Grade C

$$F_y = 46 \text{ ksi}$$

From AISC *Manual* Table 1-13, the HSS geometric properties are as follows:

HSS10.750×0.250

$$D = 10.750 \text{ in.}$$

$$t = 0.233 \text{ in.}$$

**Solution:**

Determine cross-sectional properties:

$$d = D$$

$$= 10.750 \text{ in.}$$

$$h = d - 2t$$

$$= 10.75 \text{ in.} - 2(0.233 \text{ in.})$$

$$= 10.3 \text{ in.}$$

$$A_s = \pi(dt - t^2)$$

$$= \pi[(10.75 \text{ in.})(0.233 \text{ in.}) - (0.233 \text{ in.})^2]$$

$$= 7.70 \text{ in.}^2$$

$$A_c = \frac{\pi}{4}h^2$$

$$= \frac{\pi}{4}(10.3 \text{ in.})^2$$

$$= 83.3 \text{ in.}^2$$

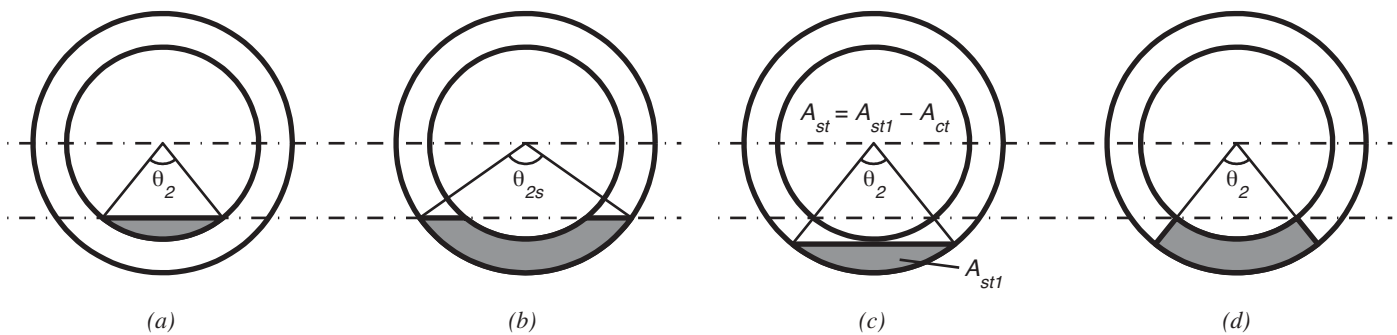


Fig. 3. Schematic of cross-sectional areas: (a)  $A_{ct}$ ; (b)  $A_{st}$ , exact; (c)  $A_{st}$ , current; (d)  $A_{st}$ , proposed.

Equation 2 is used to determine  $P_A$ :

$$\begin{aligned} P_A &= F_y A_s + 0.95 f_c' A_c \\ &= (46 \text{ ksi})(7.70 \text{ in.}^2) + 0.95(5 \text{ ksi})(83.3 \text{ in.}^2) \\ &= 750 \text{ kips} \end{aligned}$$

From AISC *Seismic Manual* Table 7-11B, Point B equations,  $h_n$  is calculated as follows:

$$\begin{aligned} K_c &= f_c' h^2 \\ &= (5 \text{ ksi})(10.3 \text{ in.})^2 \\ &= 530 \text{ kips} \\ K_s &= F_y \left( \frac{d-t}{2} \right) t \\ &= (46 \text{ ksi}) \left( \frac{10.75 \text{ in.} - 0.233 \text{ in.}}{2} \right) (0.233 \text{ in.}) \\ &= 56.4 \text{ kips} \\ \theta &= \frac{0.0260 K_c - 2 K_s}{0.0848 K_c} + \frac{\sqrt{(0.0260 K_c + 2 K_s)^2 + 0.857 K_c K_s}}{0.0848 K_c} \\ &= \frac{0.0260(530 \text{ kips}) - 2(56.4 \text{ kips})}{0.0848(530 \text{ kips})} + \frac{\sqrt{[0.0260(530 \text{ kips}) + 2(56.4 \text{ kips})]^2 + 0.857(530 \text{ kips})(56.4 \text{ kips})}}{0.0848(530 \text{ kips})} \\ &= 2.34 \text{ rad} \\ h_n &= \frac{h}{2} \sin \left( \frac{\pi - \theta}{2} \right) \leq \frac{h}{2} \\ &= \left( \frac{10.3 \text{ in.}}{2} \right) \sin \left( \frac{\pi - 2.34 \text{ rad}}{2} \right) \leq \frac{10.3 \text{ in.}}{2} \\ &= 2.01 \text{ in.} \end{aligned}$$

From AISC *Seismic Manual* Table 7-11B, Point E equations, the plastic neutral axis location,  $h_E$ , and corresponding angle,  $\theta_2$  is calculated as follows:

$$\begin{aligned} h_E &= \frac{h_n}{2} + \frac{h}{4} \\ &= \frac{2.01 \text{ in.}}{2} + \frac{10.3 \text{ in.}}{4} \\ &= 3.58 \text{ in.} \end{aligned}$$

$$\begin{aligned} \theta_2 &= \pi - 2 \arcsin \left( \frac{2h_E}{h} \right) \\ &= \pi - 2 \arcsin \left[ \frac{2(3.58 \text{ in.})}{10.3 \text{ in.}} \right] \\ &= 1.60 \text{ rad} \end{aligned}$$

Determine  $P_E$  using the current equation (Equation 4):

$$\begin{aligned}
 P_E &= P_A - \frac{1}{4} \left[ F_y (d^2 - h^2) + \frac{0.95 f'_c}{2} h^2 \right] (\theta_2 - \sin \theta_2) \\
 &= 750 \text{ kips} - \frac{1}{4} \left\{ 46 \text{ ksi} \left[ (10.750 \text{ in.})^2 - (10.3 \text{ in.})^2 \right] + \left[ \frac{0.95 (5 \text{ ksi})}{2} \right] (10.3 \text{ in.})^2 \right\} \times [1.60 \text{ rad} - \sin(1.60 \text{ rad})] \\
 &= 647 \text{ kips}
 \end{aligned}$$

Determine  $P_E$  using the proposed equation (Equation 11):

$$\begin{aligned}
 P_E &= P_A - \frac{1}{4} F_y (d^2 - h^2) \theta_2 - \frac{1}{8} 0.95 f'_c h^2 (\theta_2 - \sin \theta_2) \\
 &= 750 \text{ kips} - \frac{1}{4} (46 \text{ ksi}) \left[ (10.75 \text{ in.})^2 - (10.3 \text{ in.})^2 \right] (1.60 \text{ rad}) - \frac{1}{8} 0.95 (5 \text{ ksi}) (10.3 \text{ in.})^2 [1.60 \text{ rad} - \sin(1.60 \text{ rad})] \\
 &= 537 \text{ kips}
 \end{aligned}$$

From AISC *Seismic Manual* Table 7-11B, Point E equations,  $M_E$  is calculated as follows:

$$\begin{aligned}
 Z_{cE} &= \frac{h^3}{6} \sin^3 \left( \frac{\theta_2}{2} \right) \\
 &= \frac{(10.3 \text{ in.})^3}{6} \sin^3 \left( \frac{1.60 \text{ rad}}{2} \right) \\
 &= 67.2 \text{ in.}^3 \\
 Z_{sE} &= \frac{d^3 - h^3}{6} \sin \left( \frac{\theta_2}{2} \right) \\
 &= \frac{(10.75 \text{ in.})^3 - (10.3 \text{ in.})^3}{6} \sin \left( \frac{1.60 \text{ rad}}{2} \right) \\
 &= 17.9 \text{ in.}^3 \\
 M_E &= F_y Z_{sE} + \frac{0.95 f'_c Z_{cE}}{2} \\
 &= (46 \text{ ksi}) (17.9 \text{ in.}^3) + \frac{0.95 (5 \text{ ksi}) (67.2 \text{ in.}^3)}{2} \\
 &= 983 \text{ kip-in.}
 \end{aligned}$$

The results for the remaining points are presented in Table 1 along with an evaluation of Point E using the exact geometry (Geschwindner, 2010). These values are presented graphically in Figure 4 along with the results of the interaction diagram evaluated by dividing the cross section into many individual fibers, assuming a plastic neutral axis location, assigning a plastic stress to each fiber according to the assigned material (i.e., steel or concrete) and whether is it in tension or compression, and numerically integrating the stresses to determine pairs of axial compression and bending moment. As can be observed from Figure 4, the current formula for  $P_E$  overestimates the axial compression at Point E, which results in an unconservative approximation of the interaction diagram. Additionally, the proposed equation not only results in a close approximation of the exact results, but, because of the consistent approximations in the formulas, the pair  $(M_E, P_E)$  lies nearly on the numerically determined interaction diagram, thus introducing nearly no error to the evaluation of the interaction diagram.

To confirm the observations from Figure 4, the error between the proposed Point E and the exact interaction diagram was computed over a range of cross sections. The error in this case can be computed as a function of two nondimensional parameters: the

Table 1. Example Interaction Diagram Anchor Points		
Point	Bending Moment (kip-in.)	Axial Compression (kips)
Point A	0	750
Point E—current	983	647
Point E—proposed	983	538
Point E—exact	1,030	525
Point C	1,400	396
Point D	1,620	198
Point B	1,400	0

tube slenderness ratio,  $D/t$ , and the material strength ratio,  $F_y/f'_c$ . Given the range of compact steel tubes and material strength limitations in the *AISC Specification (2010)*, the calculations were performed for tube slenderness ratios ranging from  $D/t = 10$  to  $D/t = 125$  and material strength ratios ranging from  $F_y/f'_c = 3.5$  to  $F_y/f'_c = 25$ . The maximum error was 0.1%, which occurred for  $D/t = 10$  and  $F_y/f'_c = 3.5$ , confirming that the geometric approximation in the proposed formulas introduces nearly no error to the computation of the interaction diagram.

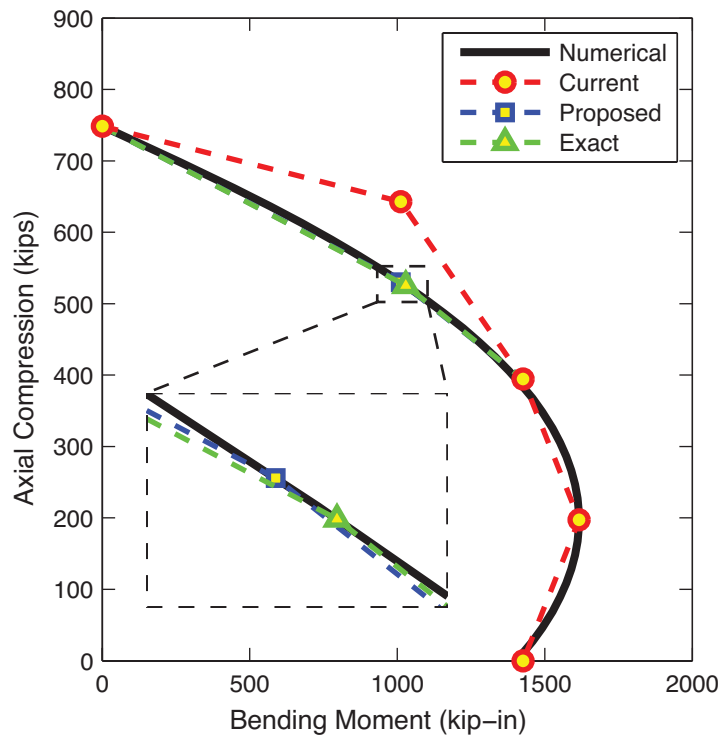


Fig. 4. Example interaction diagram.

## CONCLUSIONS

The derivation of the plastic cross-section axial strength of circular, concrete-filled steel tubes at Point E was reviewed, and the formula currently provided in the AISC *Seismic Design Manual* (AISC, 2012) and the AISC *Design Examples* (AISC, 2011) was found to be unconservative. A new formula that utilizes assumptions about the geometry that are consistent with the corresponding formula for the flexural strength at Point E was derived. This formula was verified against a numerical evaluation of the interaction surface and found to be accurate in all cases. It is recommended that this paper's Equation be adopted for use in place of the current formula in all AISC publications.

## ACKNOWLEDGMENTS

The authors thank Tiziano Perea and Louis Geschwindner for their input on this research.

## REFERENCES

- AISC (2010), *Specification for Structural Steel Buildings*, ANSI/AISC 360-10, American Institute of Steel Construction, Chicago, IL.
- AISC (2011), *Steel Construction Manual Design Examples, v14.1*, American Institute of Steel Construction, Chicago, IL.
- AISC (2012), *Seismic Design Manual*, 2nd ed., American Institute of Steel Construction, Chicago, IL.
- Geschwindner, L.F. (2010), "Discussion of Limit State Response of Composite Columns and Beam-Columns Part II: Application of Design Provisions for the 2005 AISC *Specification*," *Engineering Journal*, AISC, Vol. 47, No. 2, pp. 131–139.



# Design for Deconstruction with Demountable Composite Beams and Floor Systems

2nd Quarter 2016

JUDY LIU

## INTRODUCTION

Sustainable design, or building “green,” includes consideration of resources (e.g., energy, raw materials) but also construction and demolition waste. The statistics on waste are motivating shifts in structural design. “Current estimates in Australia have determined that approximately 40% of landfill waste is directly attributed to building and construction ... Current Australian practice in steel building construction encourage steps that structural designers can take to maximize the potential for re-using steel buildings including using bolted connections ... and ensuring easy access to connections” (Uy et al., 2015). This general approach is Design for Deconstruction (DfD). “Contrary to the conventional linear material flow, which starts with the extraction of raw materials and ends with the disposal of debris in landfills, DfD could help close this loop by reducing the cost of recovering and reusing resources” (Wang et al., 2015a).

Ongoing and recently completed research on deconstructable steel-concrete composite beams and floor systems for steel frame buildings is presented. This research includes demountable beam-slab connectors, deconstructable composite floor systems with precast concrete planks, and lightweight modular two-way steel flooring systems.

An extensive study on connectors to enable reuse of steel and composite building components has been undertaken. Demountable beam-to-girder connections, column splices for concrete-filled tube (CFT) columns and beam-to-slab connectors for steel-concrete composite beams were investigated through detailed finite element analyses and full-scale experiments. The bolted beam-to-girder connections were analyzed to determine details (e.g., geometry of the cope) and load limits that would prevent large, plastic deformations and allow the connections to be easily demounted and

reused. A blind-bolted sleeve plate CFT column splice was designed and analyzed to determine effects of sleeve length, bolt position and reinforcement ratio on tensile strength of the splice. Research on bolt connectors for composite beams, highlighted here, has shown improved performance relative to beams with welded connectors (Uy et al., 2015). This research is led by Dr. Brian Uy, Professor and Director of the Centre for Infrastructure Engineering & Safety at the University of New South Wales, Australia.

A deconstructable composite floor system with steel framing, precast concrete planks, and bolted clamp connectors has been developed. A comprehensive investigation on design and behavior of the proposed system includes detailed finite element analyses, parametric studies, and validation testing. The full-scale pushout tests, composite beam tests, and in-plane diaphragm tests are in progress. Selected results for the pushout tests and diaphragm analyses are presented here. The principal investigator (PI) for this research is Dr. Jerome Hajar, CDM Smith Professor and Department Chair of Civil and Environmental Engineering at Northeastern University, with co-PI Mark D. Webster, a structural engineer with Simpson Gumpertz & Heger Inc.

A new, modular sandwich panel system is envisioned as another alternative to steel deck composite floors. Typical steel-concrete composite floors are designed with slabs supported by beams spanning in one direction. Reinforced concrete and post-tensioned flat slab construction are able to take advantage of two-way bending behavior to increase capacity and span lengths, resulting in low floor-to-floor heights, but lack modularity. Research is under way on a new lightweight modular steel flooring system that takes advantage of two-way bending behavior and rapid-construction/deconstruction inherent in modular systems. The principal investigator for this research is Dr. Matthew Fadden, AISC Milek Fellow and an Assistant Professor at The University of Kansas.

## DEMOUNTABLE BEAM-SLAB CONNECTORS

Bolt connectors can be used in place of welded shear connectors for composite beams that are deconstructable, or

---

Judy Liu, Ph.D., Research Editor of the AISC Engineering Journal, Professor of Civil and Construction Engineering, Oregon State University, Corvallis, OR. Email: Judy.Liu@oregonstate.edu

---

demountable, as shown in Figure 1 for a beam with metal deck. Limited studies on bolted connectors for composite beams were conducted by Lam and Saveri (2012) and others. Additionally, post-installable bolted connectors were investigated by Kwon et al. (2009) for retrofit of noncomposite bridge girders. Meanwhile, pushout tests on bolted connectors conducted by Mirza et al. (2010) demonstrated shear capacity comparable to that of welded headed connectors. More recent research has considered bolted connectors as potential retrofit, or strengthening, options for existing beams. This work has expanded upon prior research and has also demonstrated the viability of bolted connectors for demountable composite beams (Pathirana et al., 2015). The connectors used were the same as those studied by Mirza et al. (2010) and included welded, headed shear connectors (WS) and two different types of M20–grade 8.8 blind bolts. One type of blind bolt has a collar (BB1), and the other type of blind bolt is secured with a washer and nut cast into the concrete (BB2) (Figure 2). When used for retrofitting existing noncomposite beams, connectors are bolted through holes created in the concrete and steel beam flanges. The holes are then filled with nonshrink structural grout (Figure 3) (Pathirana et al., 2015).

### Behavior of Demountable Beam-Slab Connectors

Seven full-scale beam specimens were tested statically under four point bending (Pathirana et al., 2015). Beam span was 19.6 ft, with an 18-in.-deep steel I-beam. The 6-in.-thick, 3.28-ft-wide concrete slab was reinforced with N12 (0.5-in. diameter) longitudinal and transverse bars at 9.45-in. spacing. One beam was noncomposite, and three composite beams were constructed with each of the three connectors; specimens CWS-ST, CBB1-ST and CBB2-ST used connectors WS, BB1 and BB2, respectively. Three specimens (CWS-RT, CBB1-RT and CBB2-RT) were constructed originally as noncomposite beams and then retrofitted with each of the connectors. Beam specimens all used 27 shear connectors in a staggered pattern. For the welded connector specimen, this would correspond to a partially composite beam design, with approximately 50% of the connectors required for fully composite beams (i.e., a shear connection ratio of 0.5). The grout hole sizes in the retrofitted specimens corresponded to the geometry and installation requirements of the connector: 3.94-in., 2.95-in. and 1.97-in. hole diameters for the WS, BB1 and BB2 connectors, respectively.

Six pushout tests were also conducted to investigate the

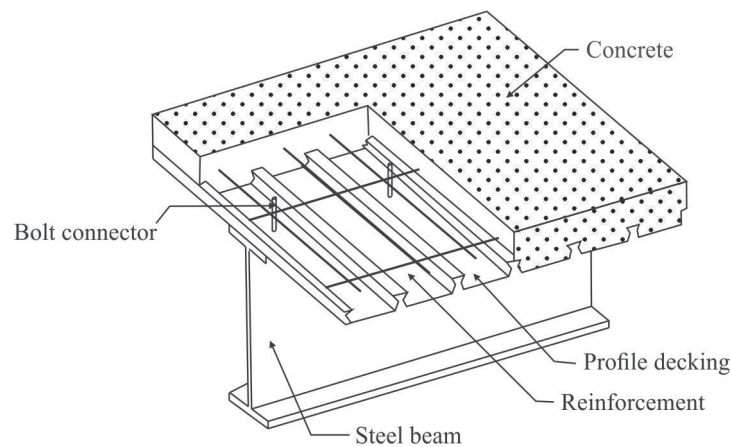


Fig. 1. Demountable composite beam with concrete on metal deck.

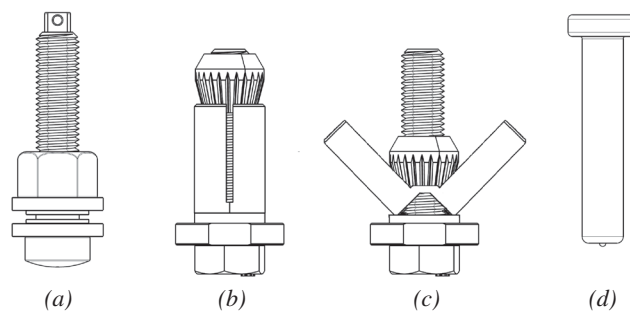


Fig. 2. (a) BB2 connector; (b) BB1 closed collar; (c) BB1 open collar; (d) WS connector.

load-slip behavior of the connectors. Each of the pushout test specimens corresponded to one of the standard (ST) composite beam specimens or one of the retrofitted (RT) composite beam specimens. Concrete or grout failure and welded stud failures were observed for the WS specimens (PWS-ST and PWS-RT). Concrete or grout failure was the limit state for the BB1 specimens, while the BB2 connectors failed in shear. The slip responses of the BB1 and BB2 specimens were variable; this was attributed to bolt hole clearances as well as deformations of the bolted connector components. Comparisons of the load-slip behavior of the connectors (Figure 4) revealed higher stiffnesses for the WS and BB1 connectors in the standard and retrofitted specimens. The strengths of the BB1 and BB2 connectors were comparable and, for the retrofitted specimens, were higher than that for the WS connectors. The BB2 connectors were

noted to be the most ductile, and the WS connectors were noted as having the most slip after yielding (Pathirana et al., 2015).

The load-slip behavior from the pushout tests was reflected in the composite beam tests. The retrofitted beam with the BB2 connectors was much less stiff than the other retrofitted beams. Both beams retrofitted with bolted connectors exhibited higher ultimate load capacity than the retrofitted beam with the welded connector. The load capacity of a noncomposite beam was increased by 40% with the BB2 connectors. At the serviceability deflection limit of approximately 1 in., the load capacities of all retrofitted beams were 50% higher than predicted (Pathirana et al., 2015). Overall, the research confirmed the viability of bolted connectors for both retrofit and new construction of composite beams.

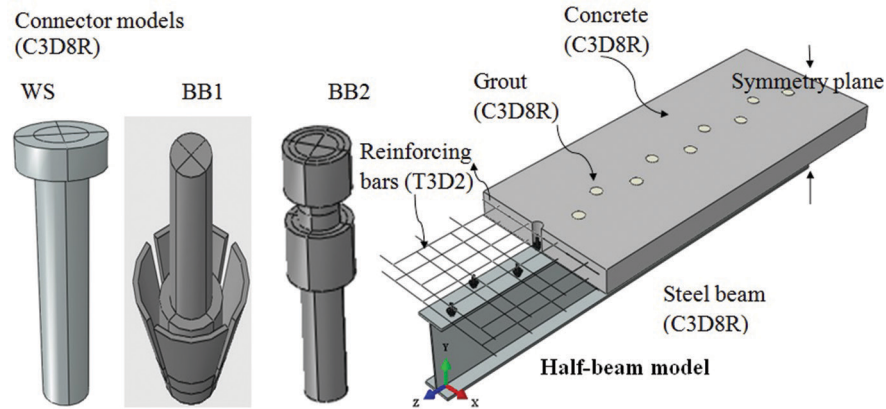


Fig. 3. Finite element model components and element types.

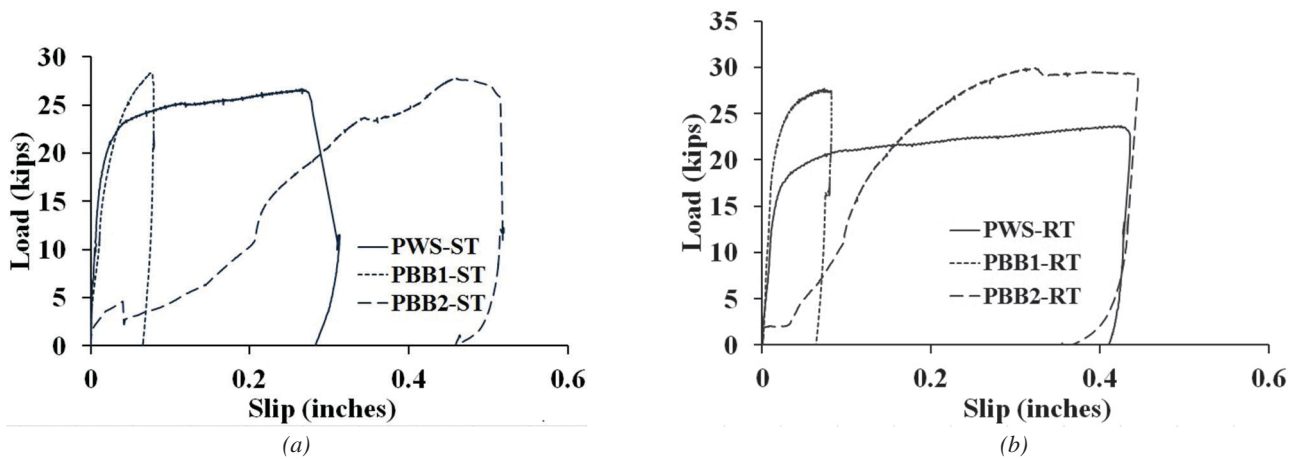


Fig. 4. Load-slip response: (a) standard condition; (b) retrofitted condition.

## Finite Element Analysis of Demountable Beam-Slab Connectors

In addition to analyses for the retrofitted composite beam specimens, Uy et al. (2015) developed detailed finite element models and conducted a parametric study of composite beams. The finite element models were composed of eight-node brick (C3D8R) and quadratic brick (C3D20R) elements for the shear connectors, concrete slab and beam. Steel reinforcement was modeled with two-node, three-dimensional truss elements (T3D2). The models allowed for comparisons of flat slabs and slabs with profiled metal decking, as shown in Figure 1; the thin steel sheeting was modeled with thin shell elements (S4R). Structural steels were modeled using elastic-plastic behavior, and the concrete was modeled with an elastic-plastic stress strain relationship with strain softening. In addition to profiled decking or flat slab, parameters investigated included concrete compressive strength and headed or bolted connectors. The bolted connectors were the type with the embedded nut. The models were validated against the experiments from Mirza et al. (2010), with good agreement on the load-slip curves, including initial stiffness that was “identical up to the ultimate load” (Uy et al., 2015).

The results of the parametric study showed increases in stiffness and strength with greater concrete compressive strengths. Use of a flat slab instead of a profiled slab also increased initial stiffness and ultimate strength. The beams with the bolted connectors were stronger than beams with the welded headed connectors, primarily due to the higher yield strength of the bolted connectors. An initial 0.04-in. slip observed in beams with the bolted connectors was attributed to the oversized holes “provided to achieve demountability in composite beams” (Uy et al., 2015).

Pathirana et al. (2015) expanded on these results with finite element models that were validated against all three of the retrofitted beam specimens. The models utilized symmetry boundary conditions to represent half of the beam. As with the models described earlier, C3D8R elements were used for the concrete, grout and steel beams; C3D20R elements were used for the shear connectors; and T3D2 elements were used for the reinforcing bars (Figure 3). A concrete damage plasticity model was used to capture the behavior of the concrete and grout. The stress-strain curves for the steel materials were represented by piecewise linear curves. Properties for the steel and concrete were based on the measured values from material property tests for the materials used in the test specimens. The finite element models again demonstrated good agreement with the experimental results. Stiffness, strength, ductility and limit states such as tensile failure of the concrete at the bottom of the slab were well predicted. Additional details of the modeling can be found in Pathirana et al. (2015).

In a parametric study, the effects of concrete compressive strength, grout strength, grout hole size and shear

connection ratio were investigated. The results confirmed that an increase in concrete compressive strength increases the ultimate capacity of the retrofitted beam. However, doubling the grout strength produces marginal increases (less than 1%) in the flexural strength of the beam. Similarly, doubling the grout hole diameter increases the ultimate strength of the beam, but this increase was not significant (less than 4%). For shear connection ratio, an increase in this ratio resulted in an increase in the ultimate capacity of the composite beam, although the rate of increase was generally less significant at higher numbers of shear connectors. Figure 5 shows the ultimate load ratio, or ultimate load normalized to that for 42 connectors (shear connection ratio of 1), versus the number of connectors. It is worth noting that the composite beam models with the BB2 connectors (CBB2) were able to develop an ultimate load ratio close to 1 (i.e., capacity of a fully composite beam) with fewer connectors than for the CBB1 and CWS models (Pathirana et al., 2015).

## Dynamic and Time-Dependent Behavior of Composite Beams with Demountable Connectors

Complementary research has been conducted on the time-dependent behavior of composite beams with blind bolts (Ban et al., 2015) and dynamic behavior of composite beams with different shear connectors (Henderson et al., 2015a, 2015b). Ban et al. (2015) conducted four full-scale tests and a computational parametric study, identifying important parameters for the long-term deflections of these composite beams, in addition to developing a finite element model capable of predicting the time-dependent behavior of composite beams with blind bolts or welded connectors. Test results from Henderson et al. (2015a) showed comparable dynamic behavior for composite beams with blind bolts and welded shear studs. The results were also used to validate a Timoshenko beam model for steel-concrete composite beams (Henderson et al., 2015b).

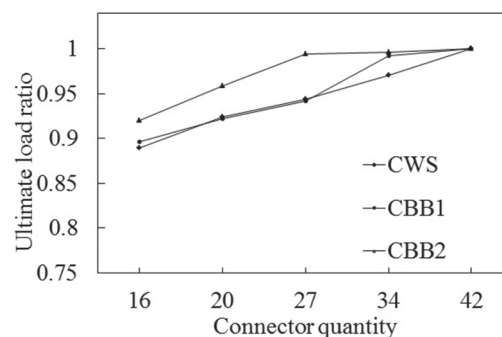


Fig. 5. Ultimate load ratio versus number of shear connectors.

## DECONSTRUCTABLE COMPOSITE FLOOR SYSTEM

Similar concepts have been used in the development of a new, deconstructable composite floor system that uses precast concrete planks and clamp connectors. This research program includes pushout tests of the clamp connectors, beam tests and diaphragm simulations. Finite element models have been used to investigate behavior of the deconstructable floor system and components, to study effects of various parameters and to inform the experimental program. Details of the floor system, finite element models and selected results from the diaphragm test finite element analyses are described. Results from some of the pushout tests are also presented.

### Details of the Deconstructable Composite Floor System

Wang et al. (2015a, 2015b) are studying deconstructable composite floor systems to enable reuse of all of the structural components. Precast concrete floor planks are attached to steel beams and girders with clamps and pretensioned bolts. The clamp connections are designed to provide composite action in the system. Channels that have been cast into the planks allow beams of any flange width to be attached at any location. Figure 6 shows a schematic of the deconstructable composite beam and cross-sections of the plank.

The planks themselves are envisioned to be 20 ft  $\times$  2 ft  $\times$  6 in., with tongue-and-groove side joints and connections designed to resist in-plane diaphragm forces. The plank size “is believed to be large enough to ensure structural integrity and reduce labor for construction and deconstruction but small enough to facilitate handling, transportation and reuse in new structures” (Wang et al., 2015b). Instead of the

conventional procedure of grouting between the planks and topping with cast-in-place concrete to achieve diaphragm shear resistance, threaded rods are used to allow for future deconstruction. The unbonded rods connect the precast planks in a staggered pattern as shown in Figure 7 and are tensioned. In this manner, friction in the joints resists the diaphragm shear, and the horizontal clamping of the panels resists joint opening due to diaphragm flexure (Wang et al., 2015b).

### Behavior of Deconstructable Clamping Connectors

To date, seven full-scale pushout tests have been conducted to investigate the strength and ductility of the clamping connectors. Prior to the pushout tests, one set of pretension tests was conducted. Several bolts were torqued until fracture to develop the relationship between the number of turns and bolt axial force and to establish pretensioning procedures for the clamps. It was determined that two complete turns of the nut provide a reliable pretension force.

The test specimens included precast concrete planks connected to WT sections representing the top portions of a W-shape beam (Figure 8a). The specimen includes a 4-ft  $\times$  2-ft  $\times$  6-in. precast concrete plank that was clamped to a WT5 $\times$ 30 or WT4 $\times$ 15.5 section. The loading was applied to the flanges of the WT sections using displacement control “to reduce eccentricity of the force application in the WT. Reaction angles are chosen to react against the concrete plank to provide realistic compressive stress distributions within the concrete” (Wang et al., 2015a). The WT4 flanges were smaller and required shims at the clamp connections. Additional parameters included the use of heavy or light reinforcement in the planks, monotonic or cyclic loading,

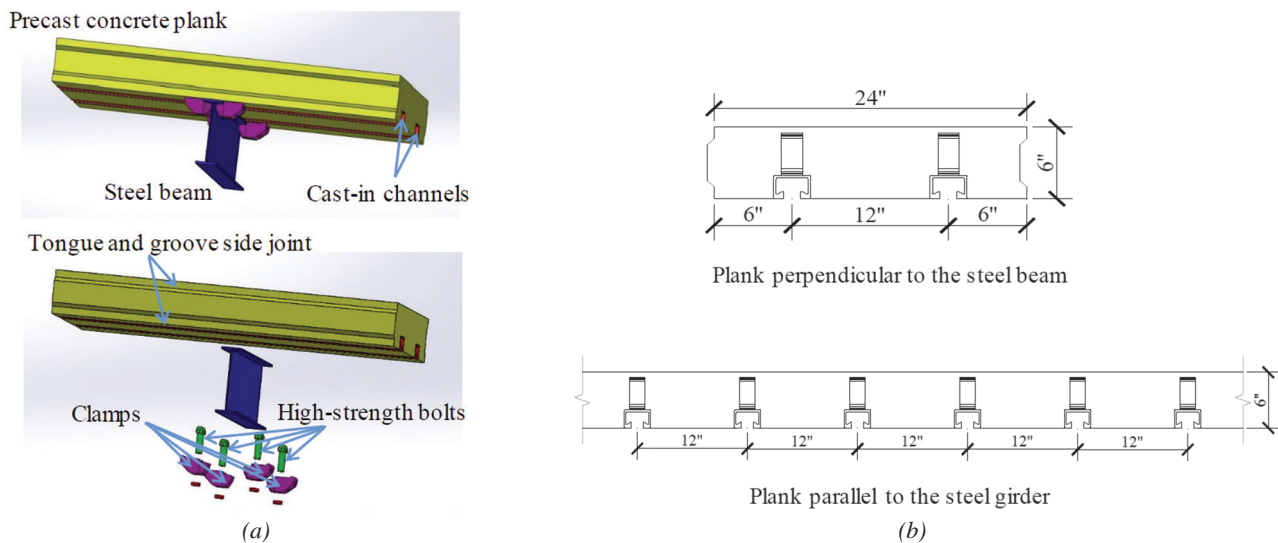


Fig. 6. (a) Deconstructable composite beam prototype; (b) precast concrete plank cross-sections.

and different bolt diameters. The light reinforcement pattern was limited to reinforcement necessary to resist gravity loading, while the heavy reinforcement pattern included additional bars to limit cracking due to concrete breakout (Wang et al., 2015a). In addition to the pushout tests, full-scale composite beam tests are designed to study the clamping connectors and the flexural strength and stiffness of the composite beams (Figure 8b).

Typical load-slip curves are depicted in Figure 9 for a monotonic pushout test and the corresponding cyclic test

with two cast-in channels and four clamps attaching the WT to the plank using 1-in. bolts. In the monotonic test, the average peak load for one clamp connector was 22.1 kips, comparable to 21.5 kips for a 3/4-in. shear stud embedded in a 4-ksi solid concrete slab. The connectors retained almost 80% of the peak capacity even at a slip of 10 in. Compared to the monotonic test results, the peak load was reduced in the cyclic test, and pinching behavior was observed, particularly at large slip values. This behavior was mainly attributed to the reduction of the frictional coefficient as a result of worn

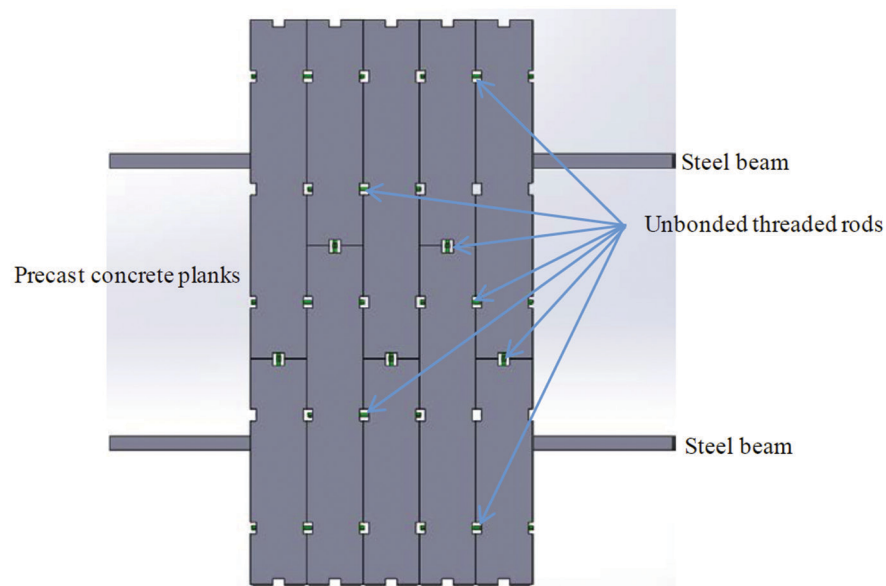


Fig. 7. Precast concrete plank layout and connections.

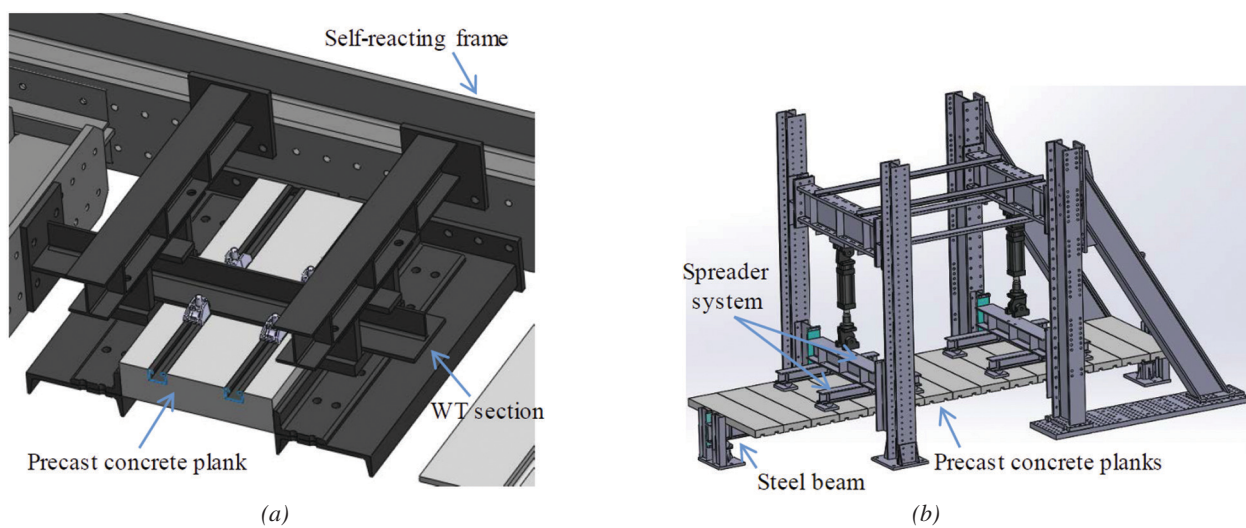


Fig. 8. Schematics: (a) pushout test setup; (b) composite beam test setup.

steel flanges and clamp teeth after several cycles. The tests were terminated when the linear potentiometer stroke was reached, and no specific limit states were observed.

### In-Plane Diaphragm Analysis of the Deconstructable Composite Floor System

To explore the in-plane shear behavior of the proposed system, a model of half of a 30-ft  $\times$  30-ft bay was created, with symmetry boundary conditions. This model was inspired by the test setup used by Easterling and Porter (1994) to study the behavior of steel-concrete composite diaphragms. The modeled diaphragm system used a W18 $\times$ 40 girder, W14 $\times$ 30 filler beams and W12 $\times$ 19 beams at the column lines (Figure 10). The W18 $\times$ 40 girder was considered to be part of the seismic force-resisting system and was, therefore, the point of application for the loading. The quasi-static, cyclic

displacement was applied after (1) compression between the planks from the threaded rods was simulated with an applied pressure and (2) bolt pretension was simulated through a change in temperature. Planks were unreinforced in the models, and they were staggered as shown in Figure 7.

The finite element analysis used a combination of eight-node reduced integration brick elements (C3D8R) and six-node reduced integration triangular prism elements (C3D6R) to represent the concrete and cast-in channels. The steel beams and concrete planks were modeled using the eight-node brick elements. The clamps and bolts were modeled using four-node tetrahedron elements (C3D4), and the steel reinforcement was represented by two-node, three-dimensional truss elements (T3D2).

Material models include a concrete damage plasticity model capable of capturing changes in stiffness with opening and closing of cracks (Wang et al., 2015b). The steel

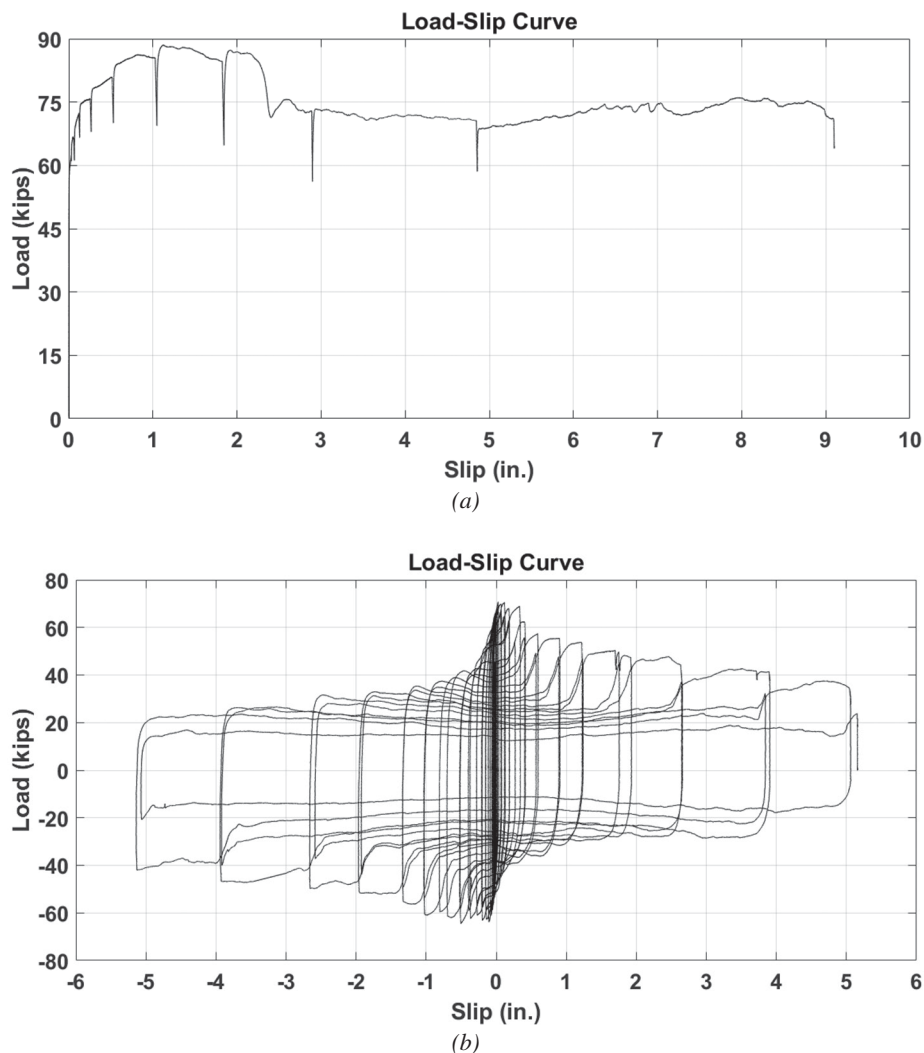


Fig. 9. Load-slip curves for specimens under (a) monotonic loading; (b) cyclic loading.

Model Number	Compressive Stress (ksi)	Number of Shear Connectors
1	0.22	28
2	0.22	20
3	0.44	28
4	0.44	20
5	0.87	28
6	0.87	20

beam, reinforcement and channels were modeled using elastic-perfectly-plastic material in both tension and compression. The bolt material was modeled following Kulak et al. (1987). Pretension was simulated by a temperature change and the resulting thermal shrinkage in the bolts. Additional details can be found in Wang et al. (2015b).

Parameters studied included the level of the compressive stress between planks and the number of shear connectors between the steel girder and the girder plank. The applied compressive stress between the planks ranged from 0.22 ksi, equivalent to tensioned rods at 4-ft spacing, to 0.87 ksi. The number of shear connectors was either 20 connectors at 3-ft spacing, representing the minimum of 25% composite action for the girder, or 28 connectors at 2-ft spacing. In total, six models with parameters as shown in Table 1 were analyzed.

The results of the analyses showed ductile behavior for all diaphragm models, with no strength or stiffness degradation. Observed limit states included joint sliding and slip of the clamps. The diaphragm shear strength increased as the compressive stress between planks increased. Joint sliding was the limit state for models 1 through 4. Slip at the clamps

was the limit state for models 5 and 6. Model 4, with fewer shear connectors, exhibited a combination of joint sliding and slip at the clamps, and was less stiff than model 3, with comparable strength. Similarly, model 6 was less strong and less stiff than model 5.

Some limit states typically observed for cast-in place concrete and conventional precast concrete diaphragms were not observed for the proposed system. No diagonal cracking was observed in the models, even though the planks were modeled with no reinforcement. The “concrete remains intact except for localized damage near the clamps” (Wang et al., 2015b). Also, the compressive stress at panel joints prevented the limit state of joint opening due to diaphragm bending.

The diaphragm parametric study, together with the push-out test results, provided valuable information for design and detailing of the proposed floor system. All of the results also showed ductile behavior at both the component and system level. Full-scale pushout, beam and diaphragm tests will further inform design guidelines and confirm the viability of this deconstructable composite floor system.

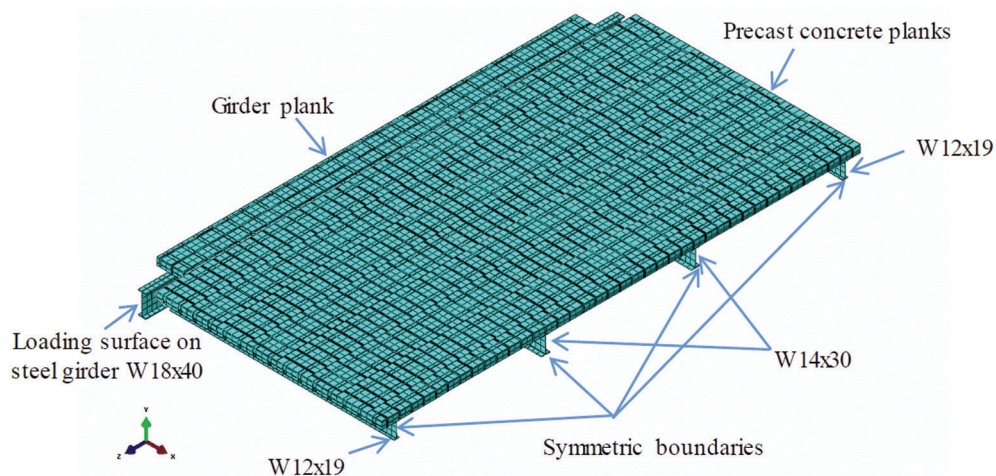


Fig. 10. Finite element model of the composite floor diaphragm.

## LIGHTWEIGHT, MODULAR, TWO-WAY, STEEL FLOORING SYSTEMS

Another alternative to conventional steel deck composite floors is a new, lightweight, modular, two-way, sandwich panel system (Figure 11) that will allow for more economical steel frames designed for reduced dead loads and seismic forces. Preliminary analysis shows that 30-ft  $\times$  40-ft bays with no filler beams are attainable with modular panels. Because this project is in an early stage, the sandwiched material is currently being modeled and optimized using finite element analysis. Possible solutions include cold-formed sections, three-dimensional space trusses or lightweight cementitious materials. It is important that the sandwiched material allows space for mechanical, electrical and fire protection equipment to optimize floor-to-floor heights and structural integration.

The modularity provides this new flooring system with advantages over traditional steel-concrete composite floors, which have significant construction and curing times. Faster construction and the possibility of deconstruction given future building use changes can reduce long-term costs and waste. Additionally, modular pieces can be shipped compactly by truck, providing transportation cost savings. Each panel will be constructed on site, bolted together and lifted into place, thus avoiding any field welding. If building use changes, deconstruction can be carried out with minimal damage to the structure by removing fireproofing and unbolting the floor system. It is even possible that panels from the floor could be deconstructed and removed while other areas of the structure remain occupied. Similarly, this modular decking system can be reconstructed for future needs. Currently, connectors are being designed and

developed to be able to resist required forces while maintaining a flat profile. Future work includes conducting full-scale experimental testing on the proposed system.

## SUMMARY

A number of options for building “green” with deconstructable composite beams and floor systems have been presented. Steel-concrete composite beams become demountable with blind bolt connectors. A comprehensive experimental and computational study confirmed the viability of these bolt connectors for retrofit and new construction of composite beams. Precast concrete planks and clamp connectors are integral to a proposed, deconstructable composite floor system. Finite element parametric studies in combination with pushout, diaphragm and beam tests, in progress, are advancing Design for Deconstruction (DfD) with this viable composite floor system. A third option for sustainable design is envisioned as a lightweight, modular, sandwich panel system that will reduce design loads, accelerate construction and accommodate building use changes. The proposed modular panel system, in early stages of development and analysis, will be validated with full-scale experiments.

## ACKNOWLEDGMENTS

Special thanks to Brian Uy, Jerome Hajjar, Mark Webster and Matthew Fadden for their contributions to this article. Sameera Pathirana, Vipulkumar Patel, Ian Henderson and Lizhong Wang also provided valuable assistance with technical content. Financial support for the research on composite beams with demountable beam-slab connectors was provided by the Australian Research Council (Discovery

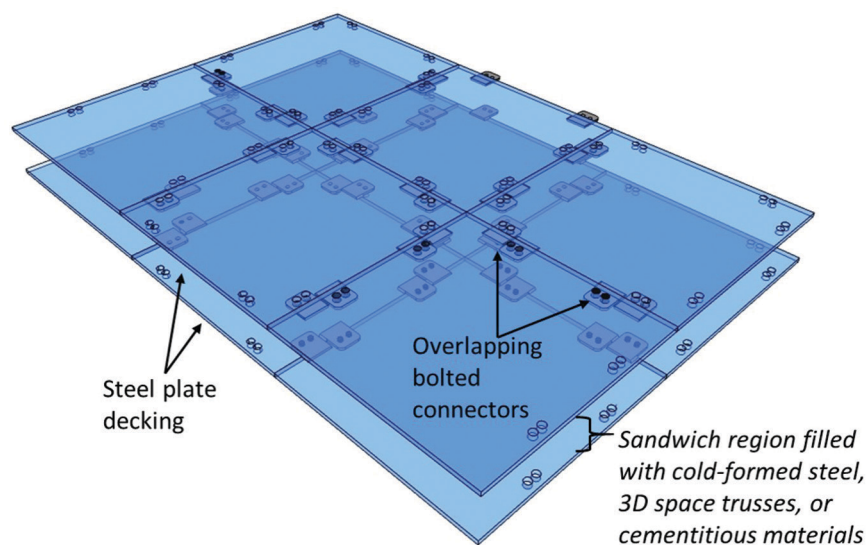


Fig. 11. Conceptual connection detail for a lightweight, modular, two-way, steel flooring system.

Grants DP110101328 and DP140102134), The University of Western Sydney, Institute for Infrastructure Engineering, and The University of New South Wales, Centre for Infrastructure Engineering and Safety. The research on deconstructable floor systems is supported by the National Science Foundation under Grant No. CMMI-1200820, the American Institute of Steel Construction, Northeastern University and Simpson Gumpertz & Heger. The American Institute of Steel Construction is supporting the research on the light-weight, modular, two-way, flooring systems through the Milek Fellowship.

## REFERENCES

- Ban, H., Uy, B., Pathirana, S.W., Henderson, I., Mirza, O. and Zhu, X. (2015), "Time-Dependent Behaviour of Composite Beams with Blind Bolts Under Sustained Loads," *Journal of Constructional Steel Research*, Vol. 112, pp. 196–207.
- Easterling, W.S. and Porter, M.L. (1994), "Steel-Deck Reinforced Concrete Diaphragms. I," *Journal of Structural Engineering*, Vol. 120, pp. 560–576.
- Henderson, I.E.J., Zhu, X.Q., Uy, B. and Mirza, O. (2015a), "Dynamic Behaviour of Steel–Concrete Composite Beams with Different Types of Shear Connectors. Part I: Experimental Study," *Engineering Structures*, Vol. 103, pp. 298–307.
- Henderson, I.E.J., Zhu, X.Q., Uy, B. and Mirza, O. (2015b), "Dynamic Behaviour of Steel–Concrete Composite Beams with Different Types of Shear Connectors. Part II: Modelling and Comparison," *Engineering Structures*, Vol. 103, pp. 308–317.
- Kulak, G. L., Fisher, J.W. and Struik, J.H. (1987), *A Guide to Design Criteria for Bolted and Riveted Joints*, Wiley, NY.
- Kwon, G., Engelhardt, M.D. and Klingner, R.E. (2009), "Behavior of Post-Installed Shear Connectors Under Static and Fatigue Loading," *Journal of Constructional Steel Research*, Vol. 66, No.4, pp. 532–541.
- Lam, D. and Saveri, E. (2012), "Shear Capacity of Demountable Shear Connectors," *Proc. 10th International Conference on Advances in Steel Concrete Composite and Hybrid Structures*, Singapore, July 2-4, 2012.
- Mirza, O., Uy, B. and Patel, N. (2010), "Behavior and Strength of Shear Connectors Utilising Blind Bolting," Paper presented to the 4th International Conference on Steel and Composite Structures, Sydney, Australia, July 21–23, 2010.
- Pathirana, S.W., Uy, B., Mirza, O. and Zhu, X. (2015), "Strengthening of Existing Composite Steel-Concrete Beams Utilizing Bolted Shear Connectors and Welded Studs," *Journal of Constructional Steel Research*, Vol. 114, pp. 417–430.
- Uy, B., Patel, V.I. and Li, D. (2015), "Behaviour and Design of Connections for Demountable Steel and Composite Structures," Keynote, 11th International Conference on Advances in Steel and Concrete Composite Structures, Tsinghua University, Beijing, China, December 3–5, 2015.
- Wang, L., Webster, M.D. and Hajjar, J.F. (2015a), "Behavior of Deconstructable Steel-Concrete Shear Connection in Composite Beams," *Proc. ASCE Structures Congress*, Portland, Oregon, April 23–25, 2015.
- Wang, L., Webster, M.D. and Hajjar, J.F. (2015b), "Diaphragm Behavior of Deconstructable Composite Floor Systems," *Proc. 8th International Conference on Behavior of Steel Structures in Seismic Areas*, Shanghai, China, July 1–3, 2015.